We are IntechOpen, the world's leading publisher of Open Access books Built by scientists, for scientists

4,800
Open access books available

122,000
International authors and editors

135M
Downloads

Our authors are among the

154
Countries delivered to

TOP 1%
most cited scientists

12.2%
Contributors from top 500 universities

BOOK CITATION INDEX
CLARIVATE ANALYTICS
INDEXED

WEB OF SCIENCE™

Selection of our books indexed in the Book Citation Index
in Web of Science™ Core Collection (BKCI)

Interested in publishing with us?
Contact book.department@intechopen.com

Numbers displayed above are based on latest data collected.
For more information visit www.intechopen.com

Epitaxial Oxide Heterostructures for Ultimate High-T$_c$ Quantum Interferometers

Michael I. Faley
PGI-5 (Mikrostrukturforschung) Forschungszentrum Jülich GmbH
52425 Jülich
Germany

1. Introduction

The broad range of physical properties available in metal-oxide materials is now beginning to be exploited in the form of epitaxial functional oxide thin-film heterostructures for the purposes of modern nanoelectronics. The discovery of high-T$_c$ superconductors and requirements for their structural perfection and chemical homogeneity also stimulated the rapid development of deposition and patterning technologies for thin films of conducting, insulating, ferroelectric, ferromagnetic and also multiferroic oxide materials. For example, epitaxial heterostructures with $SrTiO_3$ (STO) display high-mobility of charge carriers, two-dimensional interface conductivity, field-induced superconductivity, and the thermoelectric effect (see, e.g., Ohtomo & Hwang, 2004; Jia et al., 2009). The multifunctional metal-oxide heterostructures help to keep pace in shrinking dimensions down to the nanometer-scale and the increasing complexity of integrated electronic circuits, which are among the most distinctive features of modern times. Rapid progress in general purpose applications of the metal-oxide heterostructures has, in turn, supported further development of high-T$_c$ superconducting devices. Up to now, the most advanced high-T$_c$ superconducting epitaxial oxide thin-film heterostructures include thin films of $YBa_2Cu_3O_{7-x}$ (YBCO) superconductor and the technologically compatible with it metal-oxide materials whose crystal structures are mainly derived from perovskite-type crystal structures. All-oxide heterostructures based on high-quality epitaxial YBCO thin films with other metal-oxide layers are indispensable for high-T$_c$ superconducting quantum interference devices (SQUIDs) with the highest possible magnetic field sensitivity at 77 K.

SQUIDs are used for ultrasensitive electric and magnetic measurements of all physical quantities that can be converted into magnetic flux, for example, magnetic field, magnetic field gradients, current, voltage, displacement, magnetic susceptibility etc. SQUIDs serve as extremely sensitive magnetic field sensors for biomagnetic measurements, geomagnetic survey, non-destructive evaluation, low-noise preamplifiers, picovoltmeters, etc. (see, e.g., Kleiner et al., 2004; Clarke & Braginski, 2006; Fagaly, 2006). It is important that the SQUID magnetometers measure vector components of magnetic fields. In addition, they can measure (in hardware!) spatial gradients of magnetic fields; they are able to resolve tiny changes (~1 fT) in large (~ 1 µT) signals, and have a white noise spectrum in a wide frequency range (1 Hz – 10 MHz). No other magnetic field sensor has this combination of properties, which are especially important for, e.g., biomagnetic applications. Biomagnetic

applications demand a very challenging tasks of measurements of tiny magnetic fields generated by very weak ionic currents in biological neural networks and the real time inverse calculations for the localization of these ionic currents.

High-T_c superconductors have significant potential for further developments in fundamental physics and applications (Faley, 2010c). Increased interest in the high-T_c superconducting devices is spurred by the expected up to 30-fold price increase for liquid helium due to a drastic shortage of reserves (Witchalls, 2010). This will impact, first of all, the biomagnetic applications of low-T_c DC SQUIDs, for example, for magnetoencephalography (MEG), where the implementation of cryocoolers can ruin the sensitivity of measurement systems. The high-T_c SQUIDs demonstrate low noise properties up to the temperatures of about 80 K, which can be easily reached with cheap liquid nitrogen. Most of the presently available high-T_c SQUIDs are optimized for operation at a temperature 77 K, at which the equilibrium vapour pressure of liquid nitrogen coincides with atmospheric pressure. Replacement of low-T_c SQUIDs with high-T_c SQUIDs in future MEG systems would make the MEG systems independent of helium supplies, much more user-friendly, and would save up to about €100,000.- per year in operating costs per multichannel MEG system thus stimulating general acceptance of the MEG systems for clinical use. Liquid nitrogen is about ten times cheaper than liquid ^{4}He and can be easily obtained from air. It is also sufficient to replenish the liquid nitrogen in standard cryostats for MEG only about once a month and this can be done simply through a long non-magnetic silicone tube from a stationary tank placed outside the magnetically shielded room. The optional cycle refrigeration recondensing the cryogen between measurements would be also much cheaper and simpler in the case of the high-T_c MEG system compared to the low-T_c system. Also in the case of measurements of the currents of high-energy heavy-ion beams in the radioisotope beam accelerators, the implementation of high-T_c SQUID systems can save operating costs of about \$150,000 per year for each system compared to the low-T_c SQUID systems (Watanabe et al., 2010).

An important prerequisite for the application of high-T_c SQUIDs for MEG systems is magnetic field resolution better than 10 fT/√Hz down to frequencies of few Hz at 77 K. Such sensitivity of high-T_c SQUIDs has been achieved by a number of groups using superconducting multilayer flux transformers with a multiturn input coil for optimal coupling of the magnetic field to be measured to the high-T_c DC SQUID loop (Dantsker *et al.*, 1995) (Drung et al., 1996) (Faley et al., 2001, 2006b). Reduction of the excess low frequency noise of the multilayer high-T_c DC SQUID magnetometers is crucial for applications. This can be achieved only with the highest degree of crystalline perfection and stoichiometry of the high-T_c superconducting thin films in the multilayer heterostructures. The choice of the proper deposition method and deposition conditions as well as the technologically compatible materials for substrates and oxide heterostructures is important for providing the best possible epitaxial growth of all films involved (Faley et al., 2006b). Influences of lattice mismatch and difference in thermal expansion coefficients of the materials in the epitaxial oxide heterostructures should be minimized because they lead to strains inside the high-T_c superconducting films and deteriorate their properties (Faley et al., 2006a). Patterning techniques as well as proper layouts and capsulations are also essential for the total sensitivity of the high-T_c DC SQUID sensors to be optimised for particular applications.

In this chapter the technological aspects and physical properties of epitaxial oxide heterostructures are described, which are used for the preparation of high-T_c DC SQUID

flip-chip magnetometers with multilayer flux transformers having magnetic field sensitivity below 10 fT/√Hz. Deposition and structuring are outlined for the epitaxial oxide heterostructures; materials for substrates, epitaxial bilayer buffer, Josephson junctions and multilayer flux transformers; the ramp-type and bicrystal Josephson junctions; operation features, layouts, and properties of the all-oxide epitaxial multilayer high-T_c DC SQUID sensors including their encapsulation.

2. Deposition of epitaxial metal-oxide heterostructures

Significant technological efforts are required to produce high-quality samples of superconducting cuprates due to their sensitivity to the compositional and structural inhomogeneities. Accurate stoichiometry, high degree of crystallization in a single phase and proper oxidation of the film are essential. For the deposition of epitaxial YBCO films it is also important to have an appropriate substrate temperature and definite partial oxygen pressure. The required purity of c-axis orientation and 123 phase of the YBCO-films is determined by the position of the sputtering conditions in the P_{O2}-T phase diagram of YBCO. The best YBCO films are obtained along the line in the P_{O2}-T phase diagram (Hammond & Bormann, 1989) associated with initial oxygen content O_6, which corresponds to the absence of oxygen in the plane of the CuO chains and the CuO_2 planes of YBCO are undoped. Three reproducible deposition methods for the fabrication of thin-film metal-oxide heterostructures fulfilling such conditions are now mainly used: pulsed laser deposition, reactive co-evaporation, and the high oxygen pressure magnetron sputtering technique. These methods are briefly reviewed below with the emphasis on the high oxygen pressure magnetron sputtering technique, which we preferentially employ for preparation of SQUID sensors.

The reactive co-evaporation method was adopted for YBCO films by Kinder and co-workers (Prusseit et al., 2000). By rapid cycling between deposition and oxygen reaction they combined deposition in a high vacuum environment and oxygenation at a differentially high oxygen pressure enclosed in the heater. The reactive co-evaporation method is especially effective for the commercial large-scale production of epitaxial cuprate films on large wafers or on tapes intended for high current applications such as cables for transmission power lines, generators, and motors. The reactive co-evaporation method provides very high material utilization efficiency, high deposition rate, possibility of continuous deposition on km-long tapes, enabling easy switching between many elements, and fine adjustment of the composition. One of the disadvantages of the reactive co-evaporation method is the necessity of continuous rate control for each element of the compounds. An atomic absorption monitor can be used for continuous measurement of the vapour densities near to the substrates (Matias et al., 2010). The standard apparatus for reactive co-evaporation is relatively expensive with respect to initial investments and maintenance.

Pulsed laser deposition (PLD) is the most widely used method for the deposition of metal-oxide heterostructures. The material that is to be deposited is vaporized from the target by a pulsed laser beam and transported in a plasma plume to a substrate. This process can be performed in the presence of oxygen as a background gas to oxygenate the deposited metal-oxide films. The physical phenomena of laser-target interaction and film growth are quite complex. The energy of the laser pulse is first converted into electronic excitation and then into thermal, chemical and mechanical energy resulting in plasma formation, evaporation,

ablation, and, in some cases, even exfoliation. The ejected material is emitted from the target in the form of atoms, molecules, electrons, ions, clusters, and even molten globules. PLD provides a high deposition rate. A small target can be used in PLD to deposit film over large-area wafers with appropriate scanning schemes. However, this method is also relatively expensive, because a powerful laser is required. The films produced by PLD are usually relatively inhomogeneous due to ablation from a spot and contamination of the films by molten globules. There is also an angular dependence of morphology and stoichiometry of the films prepared by PLD (Sobol, 1995) (Acquaviva et al., 2005). The typical superconducting transition temperature T_c of YBCO films obtained by PLD is ≈ 89 K, which is significantly lower than $T_c \approx 93$ K obtained for bulk ceramic samples of YBCO.

The technique of sputtering at high oxygen pressures allows a smart and homogeneous on-axis in-situ deposition of high-quality metal-oxide thin films from stoichiometric targets (Poppe et al., 1990, 1992). Conventional sputtering is used extensively in the semiconductor industry to deposit thin films of various materials in integrated circuit processing. For the deposition of the epitaxial metal-oxide films it is necessary to heat the substrate to temperatures above 600 °C and introduce oxygen into the sputtering gas atmosphere. If conventional sputtering pressures of about 0.01 mbar are used for the on-axis deposition of cuprate superconductors, the negatively charged oxygen ions are accelerated towards the heated substrate by the bias potential and they thus resputter copper atoms from the deposited film leaving copper-deficient non-stoichiometric cuprate films (see, for example, Faley et al., 1991). With the high oxygen pressure sputtering technique, this problem is solved by multiple scattering of the oxygen ions at background gas pressures above 1 mbar with subsequent reduction of their kinetic energy down to thermal energies before they reach the substrate. This results in negligible backsputtering of the copper from the deposited films and, consequently, their good stoichiometry and electron transport properties. Typical superconducting transition temperature of the YBCO films obtained by this method is about 93 K and their critical current density is about 6 MA/cm² at 77.4 K.

The high oxygen pressure sputtering technique presupposes deposition at 0.5 to 5 mbar of a pure oxygen (99.999%) sputtering gas atmosphere. The main feature of the sputtering apparatus for the high oxygen pressure sputtering is the presence of a solid insulator, typically made of MACOR, between the target holder and the ground shield. The solid insulator prevents short circuit discharge at these relatively high sputtering pressures and a short mean free path ~ 0.1 mm of the accelerated electrons. If necessary, the entire range of deposition conditions from high-energy impact to low-energy thermalized quasi-condensation is accessible by changing the sputtering gas pressure in this apparatus. During deposition, the substrate typically lies unrestrained on a stainless-steel heat-resistant metal plate and is heated mainly by radiation heat transfer from a metal resistive heater. The typical substrate temperature during deposition of the films depends on the material to be deposited and for YBCO is ≈ 800 °C while the heater temperature is ≈ 920 °C.

In order to prepare multilayer heterostructures it is important that all layers should be of sufficiently homogeneous thickness. In the case of sputtering, the trivial rule is that the size of the target should significantly exceed the size of the substrate. Films deposited at an oxygen pressure ≈ 3.5 mbar from 50-mm magnetron targets were only about 2.5 % thinner at the corners of square 10-mm substrates and only 15 % thinner at the perimeter of round wafers of diameter 30 mm compared to the film thickness in the middle of the substrates. At the moment, the wafers up to 30 mm in diameter can be covered with heterostructures of

such homogeneous thickness by the high oxygen pressure sputtering technique. Larger area epitaxial metal-oxide heterostructures can be produced with a proper scanning apparatus or larger magnetron targets (Faley & Poppe, 2010).

Magnetron sputtering can be used at high oxygen pressure, but it has characteristic features in conditions of very short mean free path of electrons at pressures above 1 mbar. Large targets require magnetic fields in order to stabilise the sputtering plasma and the optimum distance between magnetic poles is typically in the range between 1 mm and 5 mm (Faley & Poppe, 2010). One of the magnetic poles can be replaced by a high-μ yoke made, for example, of iron (see Figure 1a). The magnetic field of the Sm_2Co_{17} magnets in such modified target holders additionally excites the sputtering plasma at positions away from the middle and perimeter of the target where otherwise the plasma tends to localize. This optimized arrangement of the Sm_2Co_{17} magnets in the magnetron target holder is mainly intended to stabilize the plasma. Figure 1b shows an example of magnetron sputtering from a 50-mm YBCO target demonstrating an approximately 3 mm wide ring of the most intensitive plasma region observed at 3 mbar pressure of the pure oxygen sputtering atmosphere.

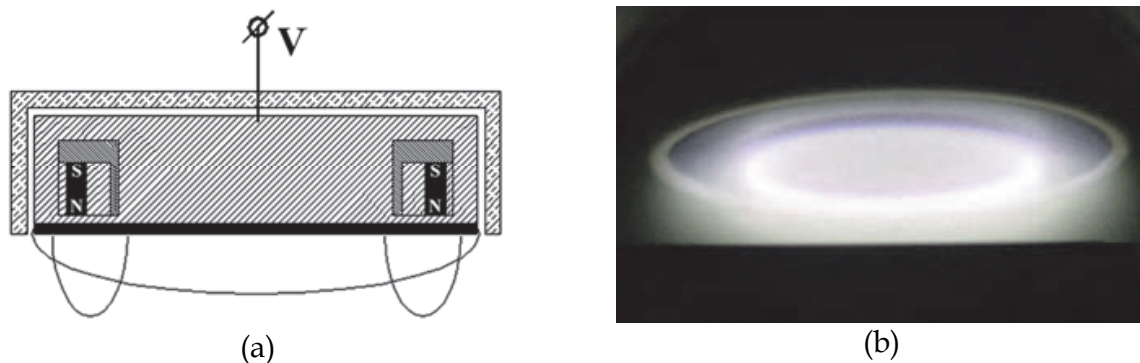(a)   (b)

Fig. 1. High oxygen pressure magnetron sputtering: (a) sketch and (b) photograph of plasma and target holder with a YBCO target and a MACOR insulator (Faley & Poppe, 2010).

The high oxygen pressure sputtering technique is suitable for the deposition of high-quality epitaxial films of all metal-oxide materials required for the production of multilayer high-T_c DC SQUID sensors. No organic material is present in the vacuum chamber of the sputtering machine. We metallize the rear of the targets with an approximately 100 μm thick silver layer, which is partially diffused into the targets at 850 °C to a depth of about 30 μm, and we bond them to the Cu holder by soldering with AgSn solder. The diffusion coefficient of Ag into bulk YBCO ceramic samples is $D_{Ag} \approx 4.5 \times 10^{-9}$ cm²/s at 850 °C (Dogan, 2005).

The base pressure in the deposition chamber for YBCO was about $2 \cdot 10^{-7}$ mbar while sputtering of YBCO was performed at ≈ 3.5 mbar pressure of pure (99.999%) oxygen. The DC sputtering technique is usually used for deposition from sufficiently conducting targets, while in the case of more insulating targets deposition is carried out by the RF sputtering technique. The typical deposition rate obtained with the DC sputtering technique was about 90 nm/hour while in the case of RF sputtering it was about 20 nm/hour.

The surface morphology of the films is crucial for the preparation of multilayer structures. Depending on the deposited material, the epitaxial growth of metal-oxide films proceeds in the following three modes: Frank-Van der Merwe growth (layer-by-layer); Volmer-Weber growth (3-D nucleation); or Stranski-Krastanov growth (mixed mode). The YBCO films grow in the Stranski-Krastanov growth mode: initial layer-by-layer growth changes to spiral

growth for films thicker than about 20 nm (Dam et al., 2002). The growth spirals on YBCO films have an average height of about 30 nm and their in-plane size strongly depends on the deposition temperature. The optimum substrate temperature is $\approx$ 100 °C higher during high oxygen pressure sputtering compared to that in the case of the PLD deposition method. This explains the width of the growth spirals of up to $\approx$ 900 nm observed on the surface of the YBCO films deposited by the high oxygen pressure sputtering technique (Faley et al., 2006b) compared to the $\approx$ 200 nm wide growth spirals on the YBCO films deposited by PLD (Dam et al., 1996). The morphology of the YBCO films is one of the factors contributing to the spread of the parameters of high-T_c bicrystal Josephson junctions with misorientation angles below 24 deg and thicknesses < 60 nm as well as to the quality of the insulation layers.

3. Materials used for the high-T_c heterostructures

For the most efficient coupling of magnetic fields to a SQUID loop, a multilayer flux transformer with at least two high-T_c superconducting epitaxial, usually, YBCO layers separated by an insulator layer is required. The technological and structural compatibility of the materials involved is an important precondition for the heteroepitaxial growth of the multilayer structures of the high-T_c SQUIDs and flux transformers. The oxygenation of the bottom YBCO films is only possible if there is sufficient mobility of oxygen ions in the insulating layer. An epitaxial buffering of substrates intended for the deposition of the high-T_c heterostructures can improve further device properties.

The non-superconducting material most compatible technologically with YBCO is $PrBa_2Cu_3O_{7-x}$ (PBCO), which has thermally activated hopping-type electrical conductivity (Fisher et al., 1994) and the perovskite-derived crystal structure is isomorphic to that of YBCO. The lattice constants of PBCO are a = 3.873 Å, b = 3.915 Å, c = 11.67 Å, which are very close to those of YBCO: a = 3.823 Å, b = 3.88 Å, c = 11.68 Å. Due to the similarity of the crystal structures of PBCO and YBCO a very low charge carrier scattering and negligible contact resistance were observed for the interfaces between the films of PBCO and YBCO (Faley et al., 1993). The PBCO films were successfully used for buffer layers, tunnel barriers, and for non-superconducting insulators in the SQUID-related heterostructures with YBCO.

It was observed that the electrical insulation in the YBCO-PBCO-YBCO heterostructures could be significantly improved by passivation of the bottom YBCO layer by a brief application of ion beam etching (Faley et al., 1997a). The reason for the increased contact resistance was a cation-disordered cubic phase of YBCO that appeared after the amorphization of the surface layer of YBCO by the ion bombardment followed by the recrystallization of this surface layer at high temperatures during the deposition of the top film (Jia et al., 1995). A further improvement in insulator resistance was achieved by implementation of a PBCO-STO electrically insulating heterostructure (Faley et al., 2010). The 50 nm PBCO film served as a buffer layer followed by the 300-nm thick STO insulator film deposited *in-situ*. The PBCO film improved epitaxial growth of the STO film over the substrate and the bottom YBCO film as well as the morphology and resistance of the insulator layer in the direction normal to the substrate surface. The resistance of the PBCO film along the substrate surface contributed to dumping of microwave resonances in the input coil of the multilayer flux transformer.

The best structural and superconducting parameters of YBCO films are typically obtained on STO substrates. Epitaxial STO films have also provided an excellent template for the epitaxial growth of the top YBCO film of the top superconducting layer in the thin film

superconducting flux transformers. Figure 2 shows the high-resolution transmission electron microscopy (HRTEM) image of the interface region between epitaxial STO and YBCO films produced by the high oxygen pressure sputtering technique and demonstrates the high-quality microstructure of these films.
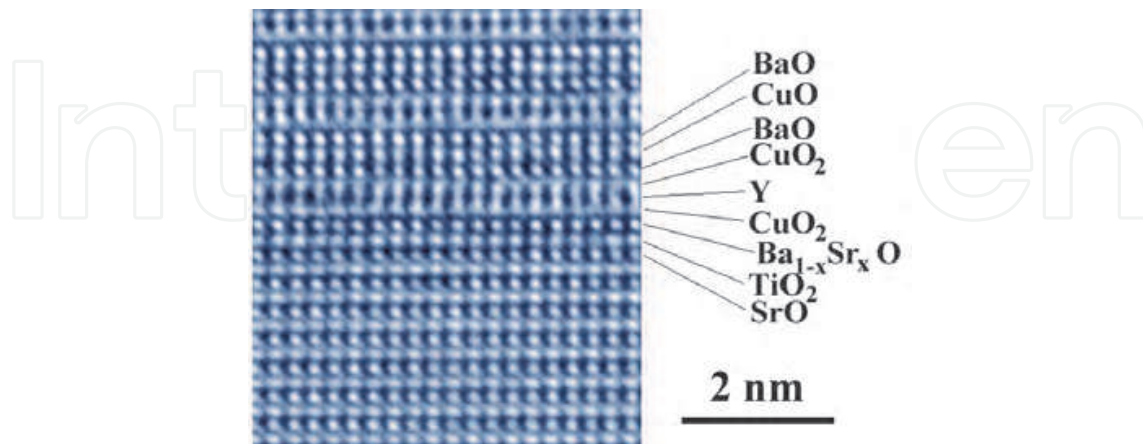

Fig. 2. Cross-sectional HRTEM image of the interface between YBCO and STO films obtained in the [110] direction (Faley et al., 2008).

Coverage of the bottom YBCO layer by the epitaxial STO films in the YBCO-STO-YBCO heterostructures does not degrade the superconducting properties of the bottom YBCO film. STO enables sufficient diffusivity of oxygen ions required for the full oxygenation of the YBCO films at, typically, about 500 °C. The diffusion coefficient of oxygen ions in single crystal STO is known to be $D_O = 5.2 \cdot 10^{-6} \cdot \exp(-11349/T)$ cm^2/sec in the temperature range between 850 °C and 1500 °C (Paladino, 1965). Assuming this dependence can be extended to lower temperatures and that the diffusivity of oxygen in STO films is similar to that in single crystal STO samples, the estimated time required to oxygenate a YBCO film covered by a 0.5 μm thick STO film is about 1.5 hour at 500 °C substrate temperature. Indeed, our empirically obtained optimum oxygenation time for the YBCO-STO-YBCO heterostructures used in the high-T$_c$ superconducting flux transformers is about 2 hours. The input coil included a 200 nm bottom YBCO film, which was covered by the approximately 400 nm PBCO-STO insulator heterostructure and 600 –1000 nm top YBCO film. A 100 nm thick silver film served to protect the top YBCO layer during structuring with AZ-photoresist.

Another useful substrate material for SQUIDs is MgO, which has a thermal expansion coefficient similar to that of YBCO ($\sim 14 \times 10^{-6}$) (see Table 1). The difference in the thermal expansion coefficients of the oxide materials such as STO, LaAlO$_3$ (LAO), NdGaO$_3$ (NGO), Al$_2$O$_3$, and YSZ often used for the substrates and films leads to a very strong tensile strain in the YBCO films degrading their superconducting properties and can even crack the films when their thickness exceeds some critical value. Much thicker multilayer high-T$_c$ thin film structures with smaller capacitance can be produced on MgO substrates. An additional advantage of MgO is that it has a relatively low dielectric constant $\varepsilon \approx 9$ and low losses tan δ $\approx 3.3 \cdot 10^{-7}$. It is one of the traditional materials used in microwave electronics. The low dielectric constant of MgO leads to a smaller parasitic capacitance through the substrate across the inductance of the DC SQUID loop compared to the DC SQUIDs on STO substrates. This leads to smaller voltage swings, but also lower white noise of high-T$_c$ DC SQUIDs on MgO substrates compared to those on STO substrates (Enpuku et al, 1996).

	Linear thermal expansion (in 10^{-6}/K)	Crystal structure	Lattice constant (Å)	Dielectric constant
MgO	~ 14	cubic, rock-salt	4.21	~ 10
BaZrO$_3$	~ 7	cubic, perovskite	4.19	~ 20
SrTiO$_3$	~ 11	cubic, perovskite	3.91	~ 270
NdGaO$_3$	~ 6	orthorhombic, perovskite	3.85	~ 20
LaAlO$_3$	~ 9	rhombohedral, perovskite	3.82	~ 24
YBa$_2$Cu$_3$O$_{7-x}$	~ 13.5	orthorhombic, perovskite	3.85	~ 5

Table 1. Selected properties of materials for substrates and buffer layers used for deposition of YBCO.

Unbuffered MgO substrates demonstrate degradation of the hygroscopic surface in air and have a large lattice mismatch of ≈ 9 % with YBCO and a crystal structure that differs from YBCO. These features usually lead to appearance of in-plane 45º misoriented grains in the YBCO films deposited on MgO substrates. The average critical current density of the YBCO films is in this case usually significantly suppressed at the boundaries between the grains and the magnetic noise of the YBCO films is drastically increased. Single-layer buffers such as BaZrO$_3$ (BZO) or STO films only slightly improved this situation. At least two buffer layers are required to deposit low-noise YBCO films on MgO: the first one should provide the epitaxial growth of films with perovskite structure on the rock-salt structure of MgO, while the second buffer layer should match the lattice constants. STO and BZO films are technologically compatible with YBCO and have the required structural properties.

An epitaxial perovskite double-layer STO/BZO buffer on MgO substrates has been developed for the deposition of low-noise and crack-free YBCO films (Faley et al., 2006a). This buffer also protects the hygroscopic surface of the MgO substrates against degradation in air and/or during the lithographic procedures. Figure 3 shows a cross-sectional HRTEM image of a BZO-STO-YBCO heterostructure deposited on a MgO (100) substrate.
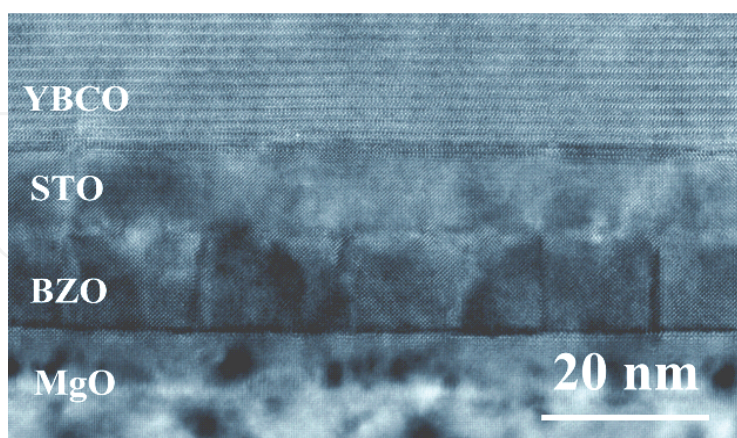

Fig. 3. Cross-sectional HRTEM image of a BZO-STO-YBCO heterostructure deposited on an MgO (100) substrate (Faley et al., 2006a).

It was observed that the antiphase boundaries (APB), which appeared at the BZO/MgO interface and spread through the BZO layer, usually disappeared at the STO/BZO interface (Mi et al., 2006). The STO layer initially grows with the lattice constant expanded to the

lattice constant of BZO ≈ 4.19 Å. However, just a after few unit cells from the STO/BZO interface the lattice constant of STO already relaxed to its bulk value ≈ 3.91 Å (see Figure 4).
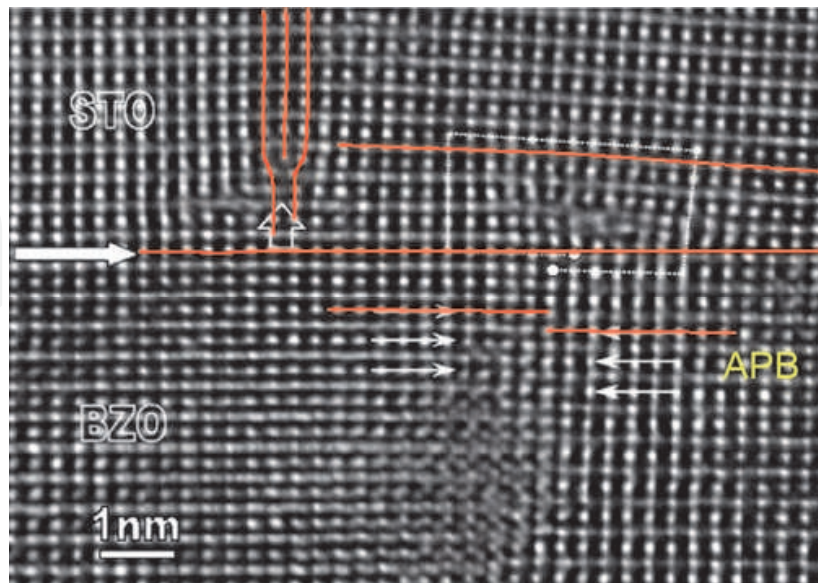

Fig. 4. Cross-sectional HRTEM image of an interface region for BZO and STO films deposited on a MgO (100) substrate (Mi et al., 2007).

Thus, at the YBCO/STO interface the lattice constant and microstructural quality of the STO layer is similar to that of the single-crystal STO substrate, but the overall thermal expansion coefficient is still determined by the 1 mm thick MgO substrate. The YBCO films deposited by high oxygen pressure sputtering technique naturally contain lattice-coherent non-superconducting Y_2O_3 nanoparticles, which are nearly spherical with a diameter of ~20 nm and are homogeneously distributed with a separation of ~30 nm (Faley et al., 2006b) and provide a strong 3D pinning of the Abrikosov vortices leading to a high critical current density J_c and a low magnetic noise in the films (Kim et al., 2007). Even 5-μm-thick YBCO films on the buffered MgO substrates do not display cracks and demonstrate a critical current density ≈ 3.5 MA/cm² at 77 K (Faley et al., 2008). The 1 cm wide films have an estimated total critical current of ≈ 1.7 kA at 77 K, which is about 17 times greater than the critical current of the present day 2nd-generation high-T_c superconducting tapes of similar width. Such high and homogeneous critical current densities of the high-T_c superconducting films are beneficial for production of the low-noise SQUID sensors, for high-Q microwave resonators and filters in communication technologies as well as for high-T_c superconducting tapes intended for the generation and transport of electrical power. The YBCO films deposited on the buffered MgO substrates demonstrated conductivity proportional to the film thickness for up to about 5 μm thick films (Faley et al., 2006a). The specific conductivity of YBCO films on other substrates such as STO, LAO, NGO, Al_2O_3, and YSZ was saturated or even dropped when the film thickness exceeded the critical values and cracks appeared in the YBCO films.

4. Patterning techniques for epitaxial metal-oxide multilayers

In the case of the epitaxial metal-oxide multilayers for high-T_c SQUIDs it is essential to avoid grain boundaries in the superconducting films because the thermally-activated hopping of flux vortices and fluctuations of superconducting current at the grain boundaries often act

as sources of flicker noise in the SQUIDs. Patterning of bottom layers should leave chemically clean and bevelled edges of the structures for the homogeneous epitaxial growth of top superconducting layers over the edges. Such structuring can be achieved by non-aqueous chemical etching as well as by the ion beam etching methods briefly described below.

Chemical etching in a Br-ethanol solution in combination with a deep-UV photolithography of PMMA photoresist was used for the patterning of YBCO-PBCO heterostructures to prepare the high-T_c Josephson junctions, crossovers, and interconnects (Faley et al., 1993). It was observed that the chemical etching of c-axis-oriented YBCO and PBCO films through a mask of PMMA photoresist is very anisotropic: it is much faster along the ab-planes than in the c-direction of the films. This causes abnormally large undercutting, which results in very gently sloping edges of the structures (see Figures 5 and 6). The angle α of slope of the edge is about 3 degree with respect to the substrate plane. This angle can be increased by extending the etching time or in combination with ion beam etching.
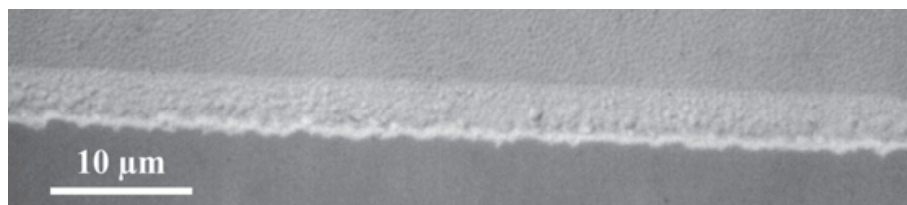

Fig. 5. Optical image of a 500-nm thick YBCO-PBCO bilayer etched through a mask of PMMA photoresist by the Br-ethanol solution. The upper part of the picture shows the film, while the lower part shows the STO substrate. The bright horizontal stripe in the middle of the picture is the chemically prepared edge.
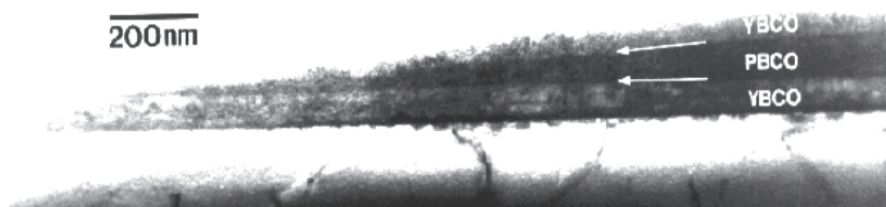

Fig. 6. A low-magnification TEM picture. This picture gives an overview of a cross-section of a YBCO-PBCO-YBCO edge structure, containing the bottom YBCO film, the insulating PBCO layer, the PBCO barrier and the top YBCO film (Faley et al., 1993).

The main advantage of the non-aqueous chemical etching in Br-ethanol solution is that the edge area is not contaminated by substrate material and shows negligible structural damage at the surface layer. Moreover, this solution does not change the local stoichiometry at the surface and, in contrast to the ion beam etching, it does not even affect the oxidation state of the copper (Vasquez et al., 1989). Bromides YBr, BaBr or CuBr are soluble in ethanol and, therefore, the surface of the edge appears to be very clean after etching followed by rinsing in ethanol. The chemical etching in Br-ethanol solution was used for the preparation of the ramp-type high-T_c Josephson junctions and the bottom layers, YBCO and PBCO, in the multilayer flux transformers with PBCO insulation layer (Faley et al., 2001). If an STO film was used for the insulation between the YBCO films, the bottom YBCO layer can also be etched by the chemical etching. The lower superconducting layer used for the return lead of the input coil

and the pick-up loop does not require high precision in structuring and it was patterned with deep-UV lithography using a PMMA-photoresist and Br-ethanol chemical etching.

Ion beam etching enables sub-micrometer precision in structuring the films through masks of AZ-type (mainly AZ5214E and AZ MIR701) photoresists. Upper superconducting layers in the ramp junctions and flux transformers contain μm-size structures and required conventional patterning with AZ photoresist and ion beam etching. Ion beam etching can be also used for structuring the bottom YBCO layer and insulation layer under condition of sufficiently low-angle edges of the photoresist mask. Proper cleaning with microstructural restoration of the edge surface should follow the etching. Bevelling of the AZ-photoresist edges down to an angle below 20 degrees relative to the substrate plane can be realized by backing-out of the photoresist at 130 °C (David et al., 1994).

Cleaning and restoration of the edge surface after etching is more difficult in the case of the ion beam etching as compared to Br-ethanol chemical etching. Rinsing and mechanical polishing in acetone and methanol followed by annealing in the presence of oxygen plasma can remove the photoresist, including carbonized parts of photoresist near the edges, as well as the amorphous materials redeposited on the edges of the photoresist structures during ion beam etching. Annealing in the presence of oxygen plasma also leads to recrystallization of the surface of edges of the etched film, which partially recovers its microstructural and electron transport properties. A high quality of the crossovers and vias in the multilayer multiturn coil of the flux transformer is essential to obtain high values of the induced superconducting current. Due to the damage-free interfaces and gently sloping edges produced by Br-ethanol etching we achieved critical currents for the flux transformers of about 100 mA at 77 K. The observed 60 μT peak-to-peak dynamic range of the magnetometer having 8-mm pick-up loop ($L_{pu} \approx 20$ nH) is limited mainly by this critical current of the flux transformer.

We use both patterning techniques – non-aqueous Br-ethanol chemical etching and ion beam etching – for the preparation of sensitive high-T_c multilayer DC SQUID sensors with reduced low frequency noise, which are described in the following sections.

5. Multilayer high-T_c DC SQUID magnetometers

In this section, the review of multilayer high-T_c DC SQUID flip-chip magnetometers will include a short introduction to the principle of operation of DC SQUIDs, a description of their noise properties and basic components: high-T_c Josephson junctions, superconducting multilayer flux transformers with multiturn input coil, and capsulation. The reproducibility of the high-T_c Josephson junctions is especially important in the case of implementation of the high-T_c DC SQUID arrays. The vacuum-tight encapsulation of the sensors is a prerequisite for their long-term stability, easier handling, and for the reduction of low-frequency noise by removing the magnetic flux trapped in the superconducting films.

5.1 DC SQUIDs – principle of operation

SQUIDs consist of a loop of superconductor interrupted by one or two Josephson junctions. The operation of SQUIDs is based on the dependence of phase shift $\Delta\varphi$ of quantum wave-functions Ψ of Cooper pairs on magnetic flux Φ passing through the SQUID loop. This dependence is caused by the fundamental dependence of the canonical momentum $\vec{p} = m\vec{v} + q\vec{A}$ and, consequently, de Broglie wavelength $\lambda = h / |\vec{p}|$ and wave vector $\vec{k} = \vec{p} / \hbar$

of charged particles on magnetic vector potential $\vec{A}$. The superconducting wave function $\Psi = |\Psi| \exp(i\varphi)$ has the spatial variation of the phase $\varphi = \varphi(\vec{r}, t)$ due to the presence of the vector potential $\vec{A}$ of the magnetic field threading through the SQUID loop. The phase difference $\delta\varphi_{1-2}$ of the wave function at positions x1 and x2 is

$$\delta\phi_{1-2} = \int_{x1}^{x2} \vec{k} d\vec{l} = \frac{q}{\hbar} \int_{x1}^{x2} \vec{A} d\vec{l} = \frac{2\pi}{\Phi_0} \int_{x1}^{x2} \vec{A} d\vec{l} ,$$ where $\Phi_0 = h/q = h/2e \approx 2.07 \times 10^{-15}$ T·m² is the

magnetic flux quantum.

The superconducting wave function $\Psi = |\Psi| \exp(i\varphi)$ is continuous in the superconductor up to the Josephson junctions. The requirement that the superconducting wave function Ψ have a single value everywhere is an important boundary condition for SQUID operation. At the Josephson junctions, the jump of phase $\Delta\varphi$ of the wave functions in individual superconducting electrodes is detected according to the Josephson current-phase relationship $I(\varphi) = I_c \sin(\Delta\varphi)$. This quantum interference leads to a periodic dependence of the output voltage of SQUIDs on applied magnetic flux Φ threading through the SQUID loop thus enabling the SQUIDs to convert tiny changes in magnetic flux Φ into measurable voltage signals.
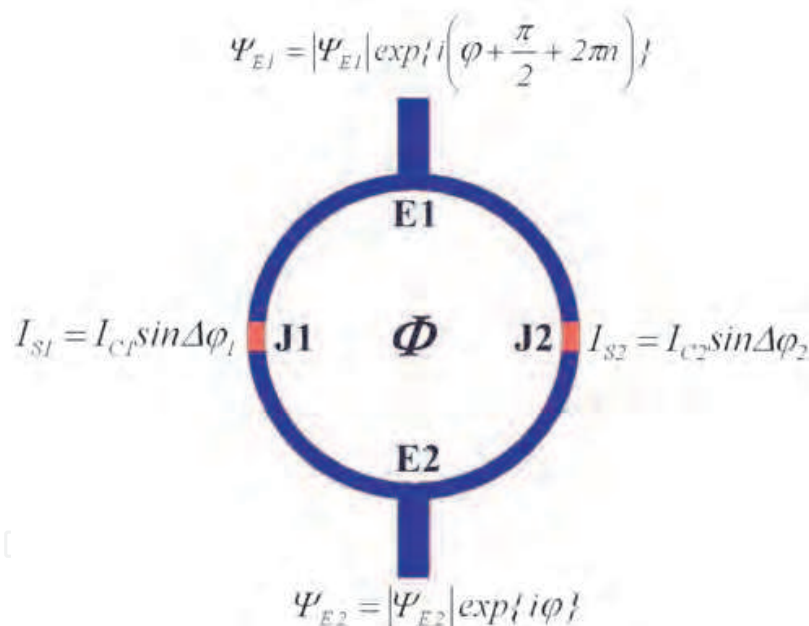

Fig. 7. Schematic representation of the DC SQUID loop with values of the superconducting wave-function Ψ, critical currents I_{S1} and I_{S2} of the Josephson junctions J1 and J2, respectively, and the magnetic flux Φ penetrating through the SQUID loop.

Direct-current SQUIDs (DC SQUIDs) consist of a loop of two superconducting electrodes E1 and E2 connected together by two Josephson junctions denoted as J1 and J2 in Figure 7. DC SQUIDs are sensitive flux-to-voltage transducers: when a flux Φ of the magnetic field penetrates the DC SQUID loop, the spatial variations of the phase of the wave function Ψ of Cooper pairs in superconducting electrodes appears. These lead to the phase shifts $\Delta\varphi_2$ and $\Delta\varphi_2$ between the wave functions in the superconducting electrodes at the Josephson junctions and, consequently, to a voltage signal on the DC SQUIDs.

The operation of DC SQUIDs can be explained most clearly in the first approximation of the zero-voltage state, for a small and symmetric DC SQUID loop. In the zero voltage state of the Josephson junctions the phase φ of the wave function of Cooper pairs does not depend on time. Without magnetic flux threading of the DC SQUID loop ($\Phi = 0$) the maximal superconducting current $I = I_{S1}+I_{S2} = I_{C1}+I_{C2}$ is achieved at the phase difference $\Delta\varphi_1 = \Delta\varphi_2 = \pi/2 + 2\pi n$ between the phases of the wave functions in electrodes at points E1 and E2 because only in this case $I_{S1}=I_{C1}$ and $I_{S2}=I_{C2}$ (see Figure 7).

Magnetic flux $\Phi = \oint \vec{A}d\vec{l} \neq 0$ changes the phase shifts $\Delta\phi_1^* = \Delta\phi_1 + \delta\phi_1 = \dfrac{\pi}{2} + \delta\phi_1 + 2\pi n$ and

$\Delta\phi_2^* = \Delta\phi_2 + \delta\phi_2 = \dfrac{\pi}{2} + \delta\phi_2 + 2\pi n$ due to the non-zero integral of the vector potential $\vec{A}$ along

the superconducting parts of the SQUID loop. The phase shifts $\Delta\varphi_1$ and $\Delta\varphi_2$ are

$\delta\varphi_1 = \dfrac{2\pi}{\Phi_0}\int\limits_{E2}^{J1} \vec{A}d\vec{l} - \dfrac{2\pi}{\Phi_0}\int\limits_{E1}^{J1} \vec{A}d\vec{l} = \dfrac{\pi\Phi}{\Phi_0}$ and $\delta\varphi_2 = \dfrac{2\pi}{\Phi_0}\int\limits_{E2}^{J2} \vec{A}d\vec{l} - \dfrac{2\pi}{\Phi_0}\int\limits_{E1}^{J2} \vec{A}d\vec{l} = -\dfrac{\pi\Phi}{\Phi_0}$, in the case of

geometrically symmetric SQUID loops like the one shown in Figure 7. Thus, in the present of a magnetic field, the phase differences at the Josephson junctions are: $\Delta\varphi_1^* = \dfrac{\pi}{2} + 2\pi n + \dfrac{\pi\Phi}{\Phi_0}$

and $\Delta\varphi_2^* = \dfrac{\pi}{2} + 2\pi n - \dfrac{\pi\Phi}{\Phi_0}$. The total maximal superconducting current through the SQUID is

thus $I = I_{S1} + I_{S2} = I_{C1}\sin(\Delta\varphi_1^*) + I_{C2}\sin(\Delta\varphi_2^*)$. In the case of Josephson junctions with similar critical currents $I_{C1} = I_{C2} = I_C$ the total current through the DC SQUID is:

$$I = I_C\left[\sin(\Delta\varphi_1^*) + \sin(\Delta\varphi_2^*)\right] = 2I_C\sin(\dfrac{\pi}{2} + 2\pi n)\cos\left(\dfrac{\pi\Phi}{\Phi_0}\right) = 2I_C\cos\left(\dfrac{\pi\Phi}{\Phi_0}\right) \tag{1}$$

at $\Phi < \Phi_0/2$. A further increase of flux changes the phase difference between the wave functions at points E1 and E2 from $\pi/2$ to $-\pi/2$ (in both cases I=0 at $\Phi = \Phi_0/2$) so that the maximal superconducting current through such DC SQUID I_{max} is always positive and is a periodic function of Φ with period Φ_0:

$$I_{max} = 2I_C\left|\cos\left(\dfrac{\pi\Phi}{\Phi_0}\right)\right| \tag{2}$$

In the dissipative regime (at bias currents $I_B > 2I_C$) there are periodic series of pulses (Josephson oscillations) of voltage U(Φ,t) across the DC SQUID. Averaging of U(Φ,t) over the period τ of the Josephson oscillations results in the dc voltage V across the DC SQUID (Tinkham, 1996):

$$V = \dfrac{1}{\tau}\int\limits_0^\tau U(\Phi,t)dt \approx \dfrac{R_N I_B}{2}\sqrt{1 - \left(\dfrac{2I_C}{I_B}\cos\dfrac{\pi\Phi}{\Phi_0}\right)^2} \tag{3}$$

where R_N is the resistance of the individual Josephson junction in the DC SQUID. The dc voltage V across the DC SQUID is a periodic function of the magnetic flux Φ through the SQUID loop.

5.2 Josephson junctions for the high-T_c DC SQUIDs

The Josephson junctions in SQUIDs transform the phase changes of the superconducting wave functions into measurable voltages owing to the Josephson current-phase relationship $I(\varphi) = I_c \sin(\Delta\varphi)$. A Josephson junction is made by sandwiching a thin layer of a non-superconducting material between two layers of superconducting material(s). With a sufficiently thin barrier, the phase of the electron wave-function in one superconductor maintains a fixed relationship with the phase of the wave-function in another superconductor. In this way, the superconductors preserve their long-range order across the insulating barrier in the Josephson junctions.

Mainly ramp-type, step edge and bicrystal grain boundary high-T_c Josephson junctions are used for high-T_c SQUIDs. The best reproducibility of the junction parameters was obtained for the ramp-type and bicrystal grain boundary high-T_c Josephson junctions shown schematically in Figure 8.
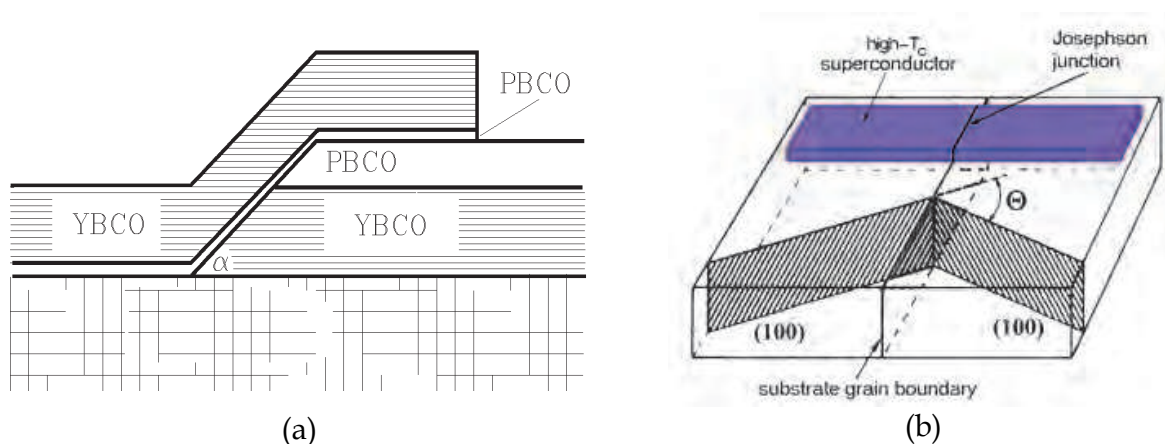

| (a) | (b) |

Fig. 8. Schematics of the ramp-type (a) and bicrystal (b) high-T_c Josephson junctions.

Ramp-type Josephson junctions contain two superconducting layers separated by a barrier layer deposited on the edge of the bottom superconducting layer (see the Figure 8a). Electron transport on the top of the bottom layer is prevented by a thick insulation layer. The barrier material and thickness can be chosen for optimum performance in particular applications. The ramp junctions on the chemically etched edges with PBCO films as the barrier and insulation layers have proven parameters that are sufficient for many applications of DC SQUIDs (Faley et al., 1995 and 1997b). The ramp junctions have the advantage that relatively cheap single crystal substrates can be used. On the other hand, compared to the bicrystal junctions, production of SQUIDs with ramp junctions is more complicated and for a similar critical current I_c their normal state resistance, R_N, is about 3 times smaller leading to smaller voltage swings of the DC SQUID. The easier production of junctions on bicrystal substrates and the smaller contribution of the noise of SQUID control electronics to the total noise of the measurement system have led to the preferred utilization of bicrystal junctions in high-T_c DC SQUIDs.

The bicrystal junctions optimized for operation in high-T_c DC SQUIDs typically have a width ≈ 1 μm, resistance $R_N \approx 6$ ohm, and a critical current $I_c \approx 25$ μA at 77 K. Dependence of the critical current density of bicrystal Josephson junctions J_c on the misorientation angle Θ can be approximated at 77 K by the following expression (Ivanov et al., 1991):

$$J_c \left(A / cm^2 \right) \cong 4.16 \cdot 10^6 \cdot \exp(-\frac{\theta(\deg.)}{4.2}) \qquad (4)$$

As was revealed by TEM studies, the effective thickness L of the distorted layer at the bicrystal grain boundary increases approximately linearly with Θ and it was suggested that the exponential decrease of $J_c(\Theta)$ is associated with this increase of the distorted layer. Typical critical current density $J_c \approx 10$ kA/cm² in the bicrystal high-T_c Josephson junctions used for DC SQUIDs operating at 77 K.

For high-T_c bicrystal Josephson junctions the resistance R_N is determined by both direct tunnelling and the resonance tunnelling components of charge carrier transport through the grain boundary (Halbritter, 1985). The total conductance of the junction with the cross-section area $\sigma = 0.2$ μm² can be approximated by the following expression (Minotani et al., 1998):

$$G = 1 / R_N \cong 2150 I_c + 11 I_c^{1/2} \qquad (5)$$

where the critical current $I_c = J_c \sigma$ is in amperes at 77 K while the resistance R_N is in ohms for the bicrystal junctions width ≈ 2 μm and the YBCO film thickness ≈ 100 nm. The second term in (5) representing the resonance tunnelling prevails at the bicrystal misorientation angles above about 24 degree. The $I_c R_N$ product is ≈ 200 μV at the bicrystal in-plane misorientation angle 24 degree and temperature 77 K:

$$I_c R_N \cong 1 / (2150 + 11 I_c^{-1/2}) \qquad (6)$$

The $I_c R_N$ product decreases with increase of the misorientation angle and corresponding decrease of the critical current density of the junction. This decrease is especially strong for misorientation angles above 24 degree, where it was found that $I_c R_N \propto \sqrt{J_c}$ (Gross et al., 1997). The critical current density J_c of symmetric 24 degree bicrystal Josephson junctions increases nearly linearly with the temperature dependence $J_c(T) \approx 10^4[4.1+6.4(60-T)/40]$ A/cm² in the range of operating temperatures T = (10 - 80) K. Noise parameter $\Gamma = 2\pi k_B T / I_c \Phi_0 = I_{th}/I_c$ for a particular junction depends strongly on the temperature: for the junctions having $I_c \approx 20$ μA at 77 K the noise parameter Γ is ≈ 0.16 at 77 K, $\Gamma \approx 0.05$ at 63 K, and $\Gamma \approx 0.005$ at 20 K.

The Stewart-McCumber parameter of the Josephson junctions $\beta_C = 2\pi I_C R_N^2 C / \Phi_0$ increases with reduced temperature and increased critical current from $\beta_C \approx 0.12$ at 77 K to ≈ 0.34 at 63 K and ≈ 1 at 20 K. Below ≈ 20 K the Josephson junctions become hysteretic. The capacitance C of the bicrystal grain boundary Josephson junction $C = \sigma \varepsilon \varepsilon_0 / t \approx 25$ fF for the junction width w = 2 μm and YBCO film thickness d = 100 nm (the junction area $\sigma = w \cdot d \approx 2$ 10^{-9} cm²). The grain boundary of the YBCO bicrystal junctions behaves as if it were mostly dielectric with an average barrier thickness t ≈ 2 nm (Winkler et al., 1994) and dielectric constant $\varepsilon \approx 28$ for the grain boundary region in YBCO (Navacerrada, 2008).

Both the noise parameter Γ and the Stewart-McCumber parameter β_C contribute to the voltage noise of the Josephson junctions (Voss, 1981) and, consequently, to the magnetic field resolution of the DC SQUID magnetometers. Reduction of temperature from the standard operating temperature of high-T_c SQUIDs 77 K to, for example, the triple point of nitrogen 63 K leads to an increase of I_c and a reduction of Γ, but also to increase of voltage noise due to the increase of β_C. An external resistive shunting of the junctions helps to reduce β_C and, consequently, voltage noise at lower temperatures and to avoid transition of the Josephson junctions to the hysteretic mode.

5.3 Performance and noise of high-T$_c$ DC SQUIDs

The average dc voltage V across the DC SQUID is a periodic function of magnetic flux Φ with the period equal to the magnetic flux quantum Φ_0. At final temperatures T > 0, the I(V) characteristics of Josephson junctions are rounded by thermal noise and the bias current I$_B$ corresponding to the maximal voltage response $|\partial V/\partial \Phi|$ is smaller than the total critical current of symmetric DC SQUID 2I$_c$ (Drung et al., 1996):

$$I_c \approx \frac{I_B}{2} + \frac{k_B T}{\Phi_0}\left(1 + \sqrt{1 + \frac{I_B \Phi_0}{k_B T}}\right) \tag{7}$$

The optimum bias current I$_B$ of high-T$_c$ DC SQUIDs is (40 ± 30) μA at 77 K. At bias currents I$_B$ > 70 μA the voltage response $|\partial V/\partial \Phi|$ is reduced due to circulation of shielding currents in the DC SQUID loop at the typical high-T$_c$ DC SQUID inductances L$_S$ of about 100 pH. The inductance L$_S$ of the DC SQUID loop reduces the voltage response to the magnetic flux in two ways: first, the induced currents shield significantly the magnetic flux through the SQUID loop at L$_S$ > $\Phi_0/2I_c$ and, second, due to the rounding of the current-voltage characteristics by thermal flux noise $\delta\Phi = \sqrt{k_B T L_S}$. At bias currents I$_B$ < 10 μA the critical currents I$_c$ < 5 μA become comparable to the thermal current I$_{th}$ = 2πk$_B$T/Φ_0 ~ 3.3 μA leading to reduction of the voltage response $|\partial V/\partial \Phi|$ of the SQUIDs. Taking into account the inductance of the DC SQUID loop L$_S$ and operating temperature T, the maximum voltage response $|\partial V/\partial \Phi|$ of DC SQUID under optimum operation conditions $\Phi \approx$ (2n+1)Φ_0/4, where n = 0, ±1..., is determined by the expression (Enpuku et al., 1995):

$$\left|\frac{\partial V}{\partial \Phi}\right| \approx \frac{4}{\Phi_0} \cdot \frac{I_c R_N}{1 + \frac{2I_c L_S}{\Phi_0}} \cdot \exp(-3.5\pi^2 \frac{k_B T L_S}{\Phi_0^2}) \tag{8}$$

Taking into account the voltage noise of the Josephson junctions, the magnetic flux noise of the high-Tc DC SQUID can be estimated according to the following expression:

$$S_\Phi = S_V \left(\frac{\partial V}{\partial \Phi}\right)^{-2} \approx 8k_B T \left[\frac{R_D^2}{R_N} + \frac{L_S^2}{4R_N}\left(\frac{\partial V}{\partial \Phi}\right)^2\right]\left[1 + \frac{1}{2}\left(\frac{2I_c}{I}\right)^2\right]\left(\frac{\partial V}{\partial \Phi}\right)^{-2} \propto \frac{L_S^2}{R_N} \tag{9}$$

for L$_S$ > 40 pH and neglecting the noise of the preamplifier of the control electronics. The dynamic resistance of the symmetric DC SQUIDs is R$_D$ = $\partial V/\partial I \approx$ R$_N$/$\sqrt{2}$ (Ryhänen et al., 1989), where R$_N$ is the normal state resistance of a single Josephson junction in the DC SQUID. At inductances L$_S$ < 40 pH the R$_D$ term in (9) prevails over the second term and the flux noise of the DC SQUID is saturated.

The white flux noise of the SQUIDs is determined mainly by the thermal fluctuations in the Josephson junctions, by the maximum voltage response to the magnetic flux $|\partial V/\partial \Phi|$ and by the noise of the preamplifier of the control electronics S$_{Ve}$:

$$S_\Phi = S_V / \left(\frac{\partial V}{\partial \Phi}\right)^2 \approx \left\{\frac{12k_B T}{R_N}\left[\frac{R_N^2}{2} + \frac{L_S^2}{4}\left(\frac{\partial V}{\partial \Phi}\right)^2\right] + S_{Ve}\right\} / \left(\frac{\partial V}{\partial \Phi}\right)^2 \tag{10}$$

at the bias current I$_B$ $\approx$ 2I$_c$.

The white flux noise of DC SQUIDs was calculated according to the expression (11) with S$_{Ve}$ $\approx$ 0.2 nV. The obtained value of the flux noise $\approx$ 3 μΦ_0/$\sqrt{Hz}$ for a 40-pH DC SQUID fits well

with the measured value $\approx 4 \ \mu\Phi_0/\sqrt{Hz}$. The inductances of the SQUID loop and other multi-layered superconducting circuits were estimated with the help of software package 3D-MLSI (Khapaev et al., 2003).

The high dynamic range of the DC SQUID measurement system is achieved by linearization of the DC SQUID output signal with the help of DC SQUID control electronics, which compensated most of the applied magnetic flux by a flux-lock-loop circuit. Operation of the DC SQUID control electronics in bias reversal mode led to an approximately 3-fold reduction in the intrinsic low-frequency noise originating from fluctuations of critical currents of the Josephson junctions in the high-T_c DC SQUIDs. As was verified, the high-T_c DC SQUID sensors are compatible with the commercially available bias-reversal DC SQUID control electronics from Tristan Technologies Inc., Cryoton Ltd., Supracon AG, Magnicon GmbH, and STL Systemtechnik Ludwig GmbH. The hybrid digital electronics provide especially high slew rate up to 5 MΦ_0/sec, dynamic range up to about 130 dB and frequency range up to about 10 MHz for the measurement system with multilayer high-T_c DC SQUIDs operating at 77 K (Ludwig et al., 2001). The above-mentioned DC SQUID electronics have the noise of preamplifier $S_{Ve} \approx (0.2 \ nV)^2/Hz$. For applications in the frequency range up to about 20 kHz, the modulation electronics with a raised transformer between the SQUID and the DC SQUID control electronics has the advantage of a convenient and stable operation of the measurement system.

5.4 High-T_c DC SQUID magnetometers with inductively coupled multiturn input coil

High sensitivity of SQUIDs magnetic fields can be provided by different superconducting flux transformers, which concentrate or convert the weak magnetic fields to be measured into the significant magnetic flux threading through the SQUID loop. The concentrating types of superconducting flux transformers such as large SQUID washer, additional single-layer thin-film concentrator or bulk flux concentrator, or direct coupled superconducting flux antenna, have relatively inefficient flux transfer and a low effective area A_{eff} caused by the large difference between the inductance of the SQUID loop $L_S \sim 80$ pH and the inductance of the concentrator pick-up loop $L_{pu} \sim 40$ nH.

Figure 9 shows the flux sensitivity $S(nT/\Phi_0) \approx 2.068/A_{eff}(mm^2)$ of the flip-chip magnetometers with multiturn input coil in comparison to one of the direct-coupled magnetometers. The effective area A_{eff} of a direct-coupled magnetometers is proportional to $A_{pu}L_S/L_{pu} \propto a$, where a is the size of the pickup coil; $A_{pu} \propto a^2$ is its area; and $L_{pu} \propto a$ is its inductance. For the single-layer directly coupled magnetometers with a pickup loop 20 mm x 20 mm, inductance of the SQUID loop ≈ 50 pH, and flux sensitivity $S \approx 4.6 \ nT/\Phi_0$, the best magnetic field resolution $\approx 24 \ fT/\sqrt{Hz}$ at 1 Hz and $\approx 14 \ fT/\sqrt{Hz}$ at 1 kHz was obtained at 77 K (Cantor et al., 1995).

Much better coupling can be achieved with a multiturn input coil, which is connected in series to the pick-up coil and inductively coupled to the SQUID loop. The effective area A_{eff} $\propto A_{pu} \cdot \sqrt{(L_S/L_{pu})} \propto a^{3/2}$ and exceeds the effective area of a direct-coupled magnetometer in about 3 times for 8 mm pick up coils and in about 10 times for 20 mm pick-up coils.

Field resolution of the inductively coupled magnetometers with multiturn input coil is:

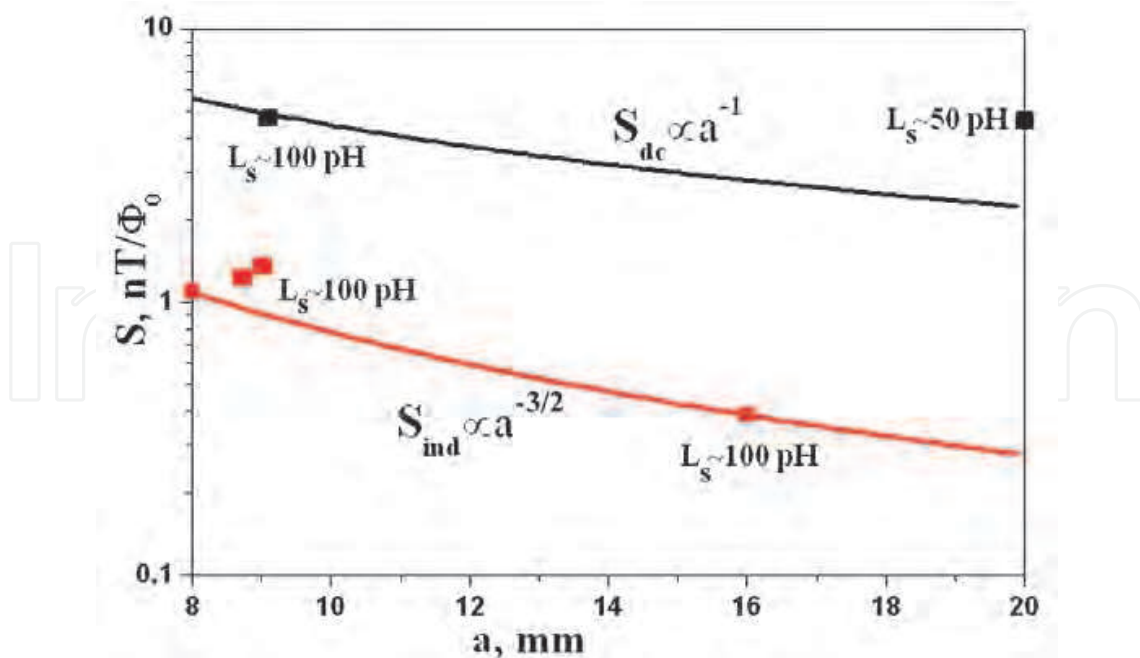$$B_N = \frac{L_{pu} + L_i}{k A_{pu} \sqrt{L_i L_S}} S_\Phi^{1/2} \propto \frac{1}{k} \sqrt{\frac{L_S}{R_N}} \tag{11}$$

Fig. 9. Flux sensitivity $S(nT/\Phi_0)$ vs pick-up loop size a(mm) for direct coupled magnetometers (■, S_{dc}) and for the inductively coupled magnetometers with multiturn input coil (■, S_{ind}) (Faley et al., 2001).

An important prerequisite for the application of high-T_c SQUIDs for MEG is a magnetic field resolution below 10 fT/√Hz at 77 K. Such magnetic field sensitivities have only been achieved with high-T_c direct current superconducting quantum interferometers (DC SQUIDs) inductively coupled to epitaxial multilayer thin-film flux transformers with a multilayer multiturn input coil. The Berkley group (Dantsker *et al.*, 1995) has demonstrated flux sensitivity S ≈ 1.7 nT/Φ_0 magnetic field resolution ≈ 27 fT/√Hz at 1 Hz and ≈ 8.5 fT/√Hz at 1 kHz using a flip-chip magnetometer with a DC SQUID inductively coupled to a multilayer flux transformer with a 9 mm x 9 mm pickup loop. Groups from Berlin and Brondby (Drung et al., 1996) jointly reported that they achieved a magnetic field resolution ≈ 53 fT/√Hz at 1 Hz and 9.7 fT/√Hz above 1 kHz for a high-T_c DC SQUID magnetometer containing a multilayer flux transformer with a 8.3 mm x 8.6 mm pickup coil integrated on the same substrate as the SQUID.

The magnetic field resolution of the high-T_c DC SQUID magnetometers was further improved to ≈ 6 fT/√Hz above 300 Hz at 77 K by implementation of a larger pick-up loop of superconducting flux transformers made on larger wafers (Faley et al., 2001). Now this resolution can be routinely obtained, while the best resolution of the high-T_c SQUID magnetometers achieved so far is about 3.5 fT/√Hz at frequencies above 100 Hz and ≈ 6 fT/√Hz at 1 Hz and the operation temperature 77 K (Faley et al., 2006a)(see Figure 10). This magnetic field resolution is similar to the sensitivity of the currently available commercial low-T_c DC SQUID magnetometers with a 21 mm pick-up loop operating at 4.2 K (see, e.g., Elektra Neuromag®, 2006) and this is sufficient for all routine applications of SQUIDs, including biomagnetic measurements such as magnetoencephalography, which are the most demanding. Figure 11 shows a sketch and photograph of the multilayer flux transformer used for the 3 fT high-T_c DC SQUID magnetometer with 16 mm multilayer flux transformer.
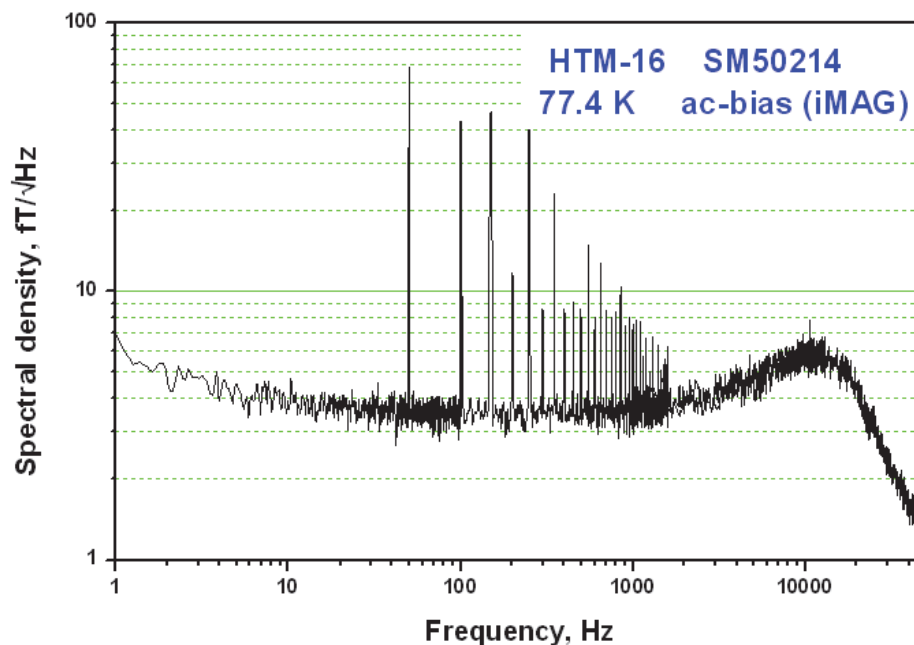
Fig. 10. Spectral density of the output signal of the measurement system based on 16-mm high-T_c DC SQUID magnetometer measured inside a 3-layer μ-metal shield and a high-T_c superconducting shield (Faley et al., 2006b).
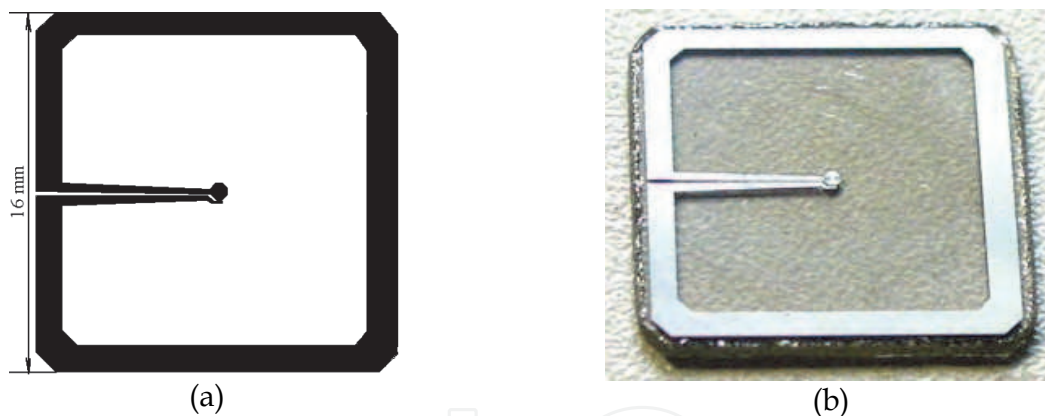

| (a) | (b) |

Fig. 11. (a) Sketch and (b) photograph of 16-mm high-T_c superconducting multilayer flux transformer with multiturn input coil in the middle intended for a 16-mm high-T_c DC SQUID flip-chip magnetometer.

The inductive coupling of the multiturn input coil of the multilayer flux transformer to the washer high-T_c DC SQUID is usually achieved by a flip-chip configuration with the SQUID and flux transformer made on separate substrates and subsequently placed together face-to-face. Single-crystal, 24° or 30° bicrystal 1 cm x 1 cm $SrTiO_3$ substrates were used to prepare the DC SQUIDs. For the preparation of the flux transformers, single crystal 10 mm x 10 mm $SrTiO_3$ substrates and $\varnothing$ 30 mm $LaAlO_3$ or $SrTiO_3$ wafers were used. For the flip-chip sensors, the SQUIDs and flux transformers with the lowest 1/f-noise were chosen and this procedure enabled the production of the best performing sensors so far.

For the flip-chip high-T_c DC SQUID magnetometers the optimum inductance of the pick-up loop $L_{pu} \approx 40$ nH is similar to the inductance of the input coil L_{in}. Reduction of the SQUID inductance down to about 40 pH does not appreciably degrade the field resolution, but

significantly improves the voltage swings and operation stability of the DC SQUID magnetometers in the magnetically unshielded environment.

The effective inductance L_{Seff} of the SQUID loop is reduced by the screening effect in the flip-chip arrangement: $L_{seff} \approx L_S \cdot [1-k^2 L_{pu}/(L_{pu}+L_{in})] \approx L_S/2$ for the coupling coefficient $k \approx 1$ (Ryhänen et al., 1989). This effective reduction of SQUID inductance leads to an increase of the voltage swings and reduction of white noise of the SQUIDs. This effect is absent in the case of direct-coupled magnetometers.

Preparation of the multilayer high-T_c DC SQUID magnetometers is more difficult and time-consuming compared to preparation of the direct-coupled magnetometers. However, this difficulty is outweighed by much better sensitivity and reproducibility of the multilayer high-T_c DC SQUID sensors. Since 1998 high-T_c DC SQUID magnetometers having the magnetic field resolution better than 10 fT/$\sqrt{Hz}$ at 77 K have already been commercially available from Forschungszentrum Jülich GmbH and Tristan Technologies Inc. (as distributor), while the commercially available direct-coupled high-T_c DC SQUID magnetometers still have the best magnetic field resolution of about 100 fT/$\sqrt{Hz}$ at 77 K.

Conventional fibre-glass cryostats typically contain aluminized Mylar foil superinsulation, which is used for thermal insulation as a shield against radiation heat transfer. Due to the Nyquist noise currents in the normally conducting Al film this foil acts as a source of magnetic field noise ≈ 2 fT/$\sqrt{Hz}$. This noise often limits the total resolution of low-T_c SQUID systems and can influence the resolution of the most sensitive high-T_c systems. Reduction of the cryostat noise will reduce further the overall noise of the SQUID measurement systems.

Nyquist noise of the integrated resistance used for damping resonances in the flux transformer is one of the possible sources of the additional flux noise. We used a PBCO-STO multilayer to construct an insulation layer between the superconducting layers of the flux transformer. This has allowed us to provide sufficient insulation and resistive properties of the insulation layer also serving as an integrated resonance-damping resistor. As a result, the V(Φ) characteristics of the magnetometers were nearly sinusoidal and the estimated contribution of the Nyquist noise of the resistor to the flux noise was below $\approx 2\ \mu\Phi_0/\sqrt{Hz}$ at 77 K. Simulations of the superconducting circuits can be performed using a personal superconductor circuit analyser (PSCAN) (Polonsky et al., 1991). Possible normal-conducting micro-shorts in the insulation layer, e.g. due to CuO precipitates or defects in epitaxial growth of the insulation layer at the edges of crossovers in the input coil, can also contribute to the white noise of the flux transformers and lead to their rejection if this noise is too high.

A non-monotonous dependence of the voltage swing on the coupling between the input coil of the flux transformer and the washer of the dc-SQUID was observed: the reduction of the insulation thickness first increased the voltage swings due to the effective reduction of the SQUID inductance down to $L_{Seff} \approx 25$ pH but the reduction of the insulation thickness below $\approx 1.5\ \mu m$ has led to a reduction of the voltage swings, the appearance of two maxima on the voltage swing, and an increase of the flux noise. Such effects indicated the shift of LC resonance in the DC SQUID to lower frequencies. This shift originated from a parasitic capacitive shunting of the DC SQUID loop by the flux transformer with the corresponding increase of the Stewart–McCumber parameter of the Josephson junctions.

The typical Stewart–McCumber parameter β_c of the bicrystal Josephson junctions is ≈ 0.3 at 77 K and it can increase significantly due to the capacitive coupling of the junctions with the return line of the multilayer flux transformer. In our geometry the increase of the capacitance prevails over the reduction of the inductance of the SQUID loop resulting in a reduction of the frequency of the LC resonance in the SQUID. At the bias current corresponding to the LC-

resonance frequency, the voltage swing can even drop to zero. However, in most cases, by keeping the insulation thickness at ≈ 1.5 μm it was possible to avoid the appearance of the LC resonance in the vicinity of the bias current of the DC SQUID while providing sufficient inductive coupling between the input coil of the flux transformer and the washer of the DC SQUID. The estimated coupling coefficient was about k $\approx \sqrt{[2(1-L_{Seff}/L_S)]} \approx 0.87$. For further improvement of the sensors a simultaneous optimization of L_S and insulator thickness is required: a further decrease in the SQUID inductance L_S and a simultaneous decrease in the insulator thickness would keep the resonance frequency unchanged.

Further improvement of sensitivity and expanding the functionalities of high-T_c sensors are possible with, for example, larger size pick-up loops in the multilayer flux transformers and implementation of serial arrays of high-T_c DC SQUIDs. For optimum field-to-flux transformation, the increase in the inductance of the pick-up loop L_{pu} should be followed by a corresponding increase in the inductance of the input coil L_{in} of the multilayer flux transformer so that $L_{pu} \approx L_{in}$. In the case of N serial input coils each with inductance L_{in} this criterion transforms into the following: $L_{pu} \approx N \cdot L_{in}$.

Theoretically, the voltage swings of the sensors increase with implementation of serial SQUID arrays proportional to the number of SQUIDs N and this also reduces the white noise of the sensors in about $\sqrt{N}$ times. At sufficiently large N, the magnetic field resolution of the high-T_c DC SQUID magnetometers with sufficiently large input coils can potentially reach values below 1 fT/$\sqrt{Hz}$ at 77 K. The crucial point for the application of high-T_c DC SQUID arrays is the reproducibility of the high-T_c Josephson junctions. With high-quality substrates and photolithography the both junction types, ramp-type junctions and bicrystal junctions, have demonstrated a spread of critical currents on a chip below 10 %, which is sufficient for the preparation of arrays of high-T_c junctions (Song et al., 2010).

Serial connection of two DC SQUIDs (dual-SQUID) is the first step in the application of high-T_c DC SQUID arrays (Chen et al., 2010). Dual-SQUIDs with bicrystal Josephson junctions demonstrate a duplication of SQUID voltage swings and a reduction of noise compared to a single SQUID sensor with similar SQUID loop inductance and parameters of the Josephson junction.

Arrays of washer-SQUIDs can be inductively coupled to a single multilayer flux transformer having corresponding number of input coils and a sufficiently large inductance of the transformer pick-up loop. We suggest to couple inductively dual-SQUIDs with large area multilayer flux transformers (see Figure 12) for further improvement of the operation parameters of the high-T_c DC SQUID magnetometers and gradiometers.
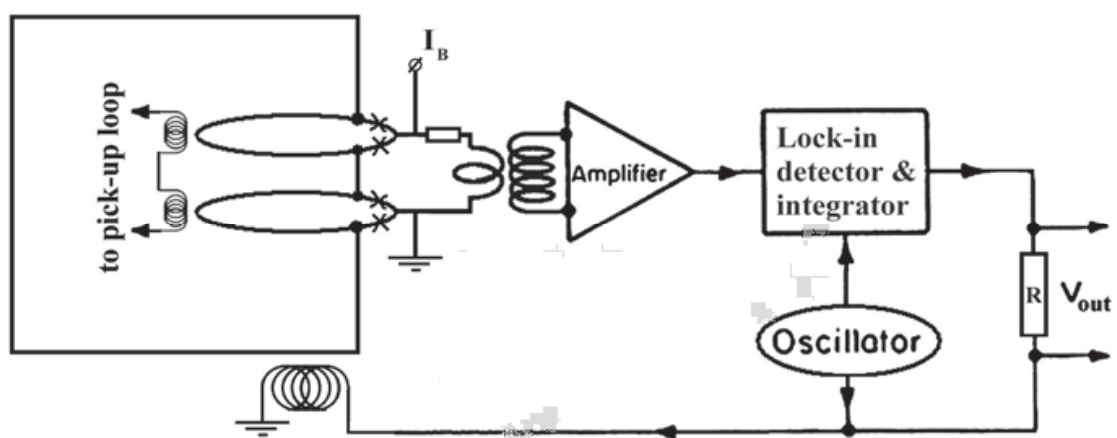

Fig. 12. Schematics of the dual-SQUID flip-chip magnetometer with control electronics.

In the suggested dual-SQUID circuit, shown schematically in Figure 12, both SQUIDs are directly coupled to a common pick-up loop, which, in turn, is inductively coupled to a feedback and modulation coil of the control electronics. The two SQUID washers are also inductively coupled to two multiturn input coils of the large-area multilayer flux transformer providing sensitivity of the sensor to the magnetic field to be measured. Application of the modulation signal to a directly coupled loop results in lower noise of the sensor. In this case, the feedback modulation signals are essentially decoupled from the pick-up loop of the multilayer flux transformer. This results in less cross-talk between the sensors compared to the case of application of the modulation signal to the pick-up coil of the multilayer flux transformer.

Further developments of the high-T_c DC SQUID sensors will include, for example, large multilayer flux transformers for more sensitive magnetometers and large-base-length gradiometers; further reduction of low-frequency noise especially for SQUIDs exposed to large permanent magnetic fields; Q-spoiler (Hilbert et al., 1985) or different types of switches (Enpuku et al., 2001, 2002), which can be used for the dissipation of parasitic circulating currents in the flux transformer during large changes of the external magnetic fields. The switches allow sensitive measurements with the SQUID magnetometers shortly after their movement in the Earth's field or after the application of strong excitation fields for low-field magnetic resonance measurements. This can be potentially used in low field magnetic resonance measurement systems for spectroscopy, biology, or security applications (Liao et al., 2010) (Espy et al., 2005, 2010).

5.5 Encapsulation of the high-T_c DC SQUIDs

The high-T_c SQUID sensors need to be encapsulated to ensure a long and reliable service life. This is especially important for the flip-chip sensors with multilayer flux transformers. The encapsulations provide mechanical and chemical protection of the sensors thus significantly simplifying handling of the sensors during characterization, applications, and for the end-users. The vacuum-tight sealing prevents the high-T_c SQUID sensors from degradation by ambient atmosphere and humidity.

The best results are obtained with enclosure of the sensors in fibreglass epoxy encapsulations. Such packaging includes the SQUID with the multilayer flux transformer as well as heater, RF filters, and a feedback coil. The thin-film Pt resistor PT-100 serves both as a thermometer and as a heater. The heater allows easy removal of trapped magnetic flux to improve the low frequency noise properties of the sensor. Good passivation was also obtained by pouring high-T_c DC SQUIDs into non-corrosive one- or two-component silicone elastomers. However, the fibreglass capsule has the advantage that, if necessary, it can be easily opened for correction or repair of the sensor followed by recapsulation.

The size and shape of the encapsulation are usually adapted to the sensor and to the specific measuring systems intended for different applications. As examples, Figure 13 shows a magnetometer and a gradiometer encapsulated into the fibreglass encapsulations. Typically, the magnetometers and gradiometers are enclosed vacuum-tight in the button-shaped encapsulations like the one shown in Figure 13a.

In the case of the flux transformers with sufficiently large-area pick-up loop, the fibre-glass capsulation can have one or two holes (Fig.13b) with vacuum-tight walls inside to permit a ferromagnetic antenna to freely tread through the pick-up coil of the thin-film flux transformer to provide better coupling to an external magnetic flux source. Such cryogenic
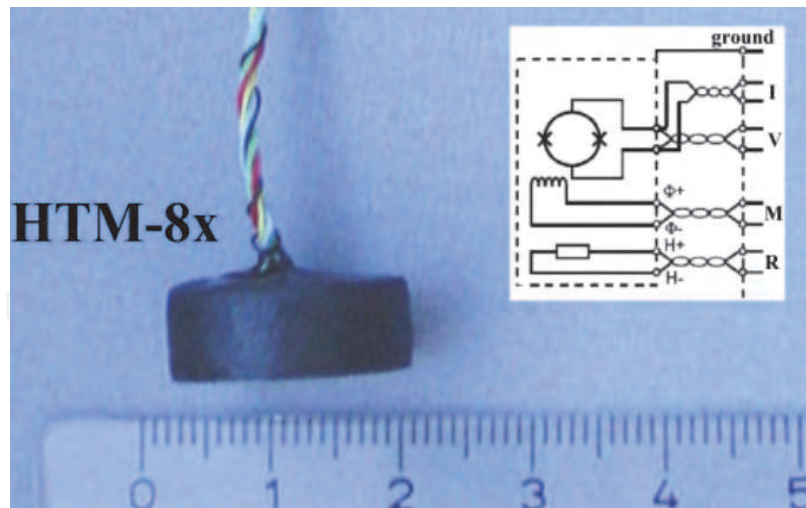
(a)
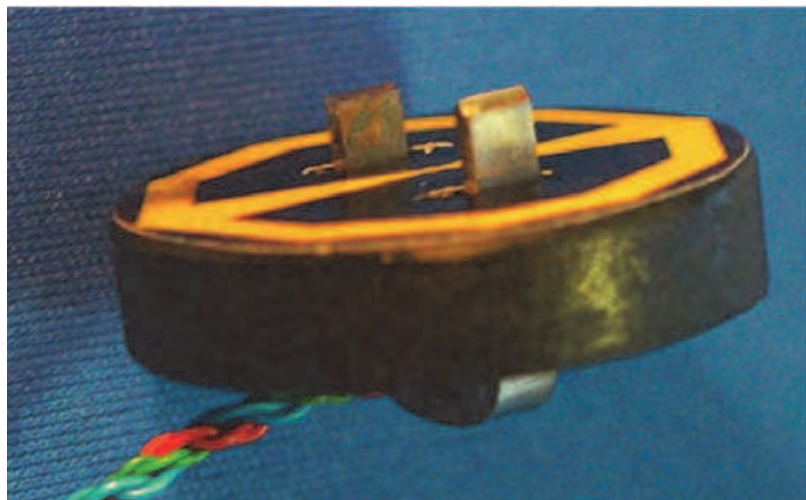
(b)

Fig. 13. Photograph of an encapsulated high-T_c DC SQUID magnetometer (a) and an encapsulated gradiometer with a ferromagnetic flux antenna (b).

gradiometer with ferromagnetic flux antenna can be used, for example, to measure the current of a beam of high-energy heavy-ion beams (Watanabe et al., 2004, 2010) and, potentially, it can be used in SQUID read-outs for a hot-electron microbolometer (Tarasov et al., 2002). The ferromagnetic antenna can be made from insulated Permalloy wires to suppress the circulation of macroscopic thermal (Nyquist) currents in the antenna associated with magnetic field noise.

6. Applications of the high-T_c DC SQUIDs with multilayer flux transformers

The high-T_c DC SQUIDs with superconducting thin-film multilayer flux transformers have found many applications thanks to their sensitivity, reproducibility, and relatively high operating temperature. The measurement systems equipped with the high-T_c DC SQUID sensors are used mainly for biomagnetic measurements, geomagnetic surveys, non-destructive evaluations, electronics technology, fundamental physics, and in

materials science. We have developed, produced, and supplied for integration in different measurement systems worldwide more than one hundred of high-T_c SQUID sensors. These requests, in turn, supported the further development of high-T_c sensors: more than 20 types of high-T_c DC SQUID magnetometers and gradiometers prepared by the high oxygen pressure sputtering technique are now available from Forschungszentrum Jülich GmbH.

The epitaxial oxide heterostructures were used in different types of SQUID microscopes (Faley et al., 2004) (Poppe et al., 2004); in a SQUID monitor for measuring the beam current of accelerator radioisotope ions (Watanabe et al., 2004, 2010); for geomagnetic surveys (Chwala et al., 1999, Clem et al., 2001, Fagaly, 2006); for non-contact testing of semiconductor structures with a SQUID laser microscope (Daibo et al., 2002, 2005); in the NDE systems for eddy current testing of aircraft wheels and rivets (Grüneklee et al., 1997); for magnetic inspection of prestressed concrete bridges (Krause et al., 2002); for picovoltmeters (Faley et al., 1997b); and for the localization and identification of deep-seated artificial defects such as holes, slots and cracks in multilayer reinforced carbon fibre polymer panels by eddy current SQUID NDE (Valentino et al., 2002) and for magnetocardiography (MCG) measurements (Drung et al., 1995; Faley et al., 2002). Biomagnetic measurements are among those general-purpose applications for which the SQUID measurement systems are preferred due to their sensitivity and ability to measure vector components of magnetic fields. The high-T_c DC SQUID magnetometers with multilayer flux transformers arranged into an axial electronic gradiometer with ≈ 1 fT/cm·√Hz at 77 K gradient sensitivity were successfully tested in a clinical environment for MCG measurements (Faley et al., 2002).

The diversity of the applications of the multilayer high-T_c SQUID sensors is astonishing. They have already proved that it is worthwhile to further develop the technology of these sensors. Other very promising applications can be potentially added but need to be tested first. The sensitivity of the high-T_c DC SQUID sensors already obtained is also sufficient for MEG measurements, but an integration of the high-T_c MEG system in an MEG laboratory is still required. Low-field magnetic resonance imaging and nuclear quadrupole resonance with multilayer high-T_c DC SQUID sensors have also many potential applications in, for example, spectroscopy, biology, and security. For example, high-T_c SQUID preamplifiers operating at intermediate temperatures ~ 20 K can be useful for readout circuits for quantum computers. Further development of specific SQUID layouts optimized for each of these and other applications will follow.

7. Summary and outlook

The technology of multilayer high-T_c DC SQUID sensors has made significant progress: their sensitivity and yield have been further improved; the sensitive sensors can be now fabricated in batch production and have been implemented on a large scale. High-T_c DC SQUID magnetometers have achieved a magnetic field resolution of about 3 fT/√Hz at 77 K, while the planar gradiometers have achieved a gradient resolution of about 10 fT/cm·√Hz at 77 K. The mature multilayer technology of the epitaxial metal-oxide heterostructures is indispensable for reaching the ultimate sensitivity high-T_c DC SQUID sensors in white noise region and can also provide high sensitivity at low frequencies. The multilayer technology of the epitaxial metal-oxide heterostructures can be also used for many other superconducting devices and for general purpose metal-oxide heterostructures.

Bilayer epitaxial buffer helps to grow thicker YBCO heterostructures with less strain. Much thicker superconducting and insulating films can be deposited. The reproducibility of the high-T_c Josephson junctions and SQUIDs achieved so far is sufficient for the effective implementation of arrays of DC SQUIDs. This improves reproducibility, increases critical current and reduces low frequency noise of the multilayer flux transformers. The final encapsulation of the sensors with integrated electronic parts such as LP filters, heater, and feedback coil additionally improves the operation, handling, and noise properties of the sensors.

The achieved magnetic field resolution, yield, and the long-term stability of the multilayer high-T_c DC SQUID sensors enable them to be integrated into multichannel MEG measurement systems. This requires installation in a proper magnetically shielded room with an MEG infrastructure and this still remains to be demonstrated. Another prospective area of application is the low-field magnetic resonance imaging (LFMRI) and combined systems MEG-LFMRI systems, both based on high-T_c multilayer DC SQUID sensors.

8. Acknowledgments

9. References

Acquaviva, S., D'Anna, E., De Giorgi, M.L., Fernandez, M., Luches, A., Majni, G., Luby, S., & Majkovacet, E. (2005). Transfer of stoichiometry during pulsed laser ablation of multicomponent magnetic targets, *Appl. Surf. Sci.*, Vol. 248, Issues 1-4, pp.286-290.

Beyer, J., Drung, D., Ludwig, F., Minotani, T., & Enpuku, K. (1998). Low-noise YBa$_2$Cu$_3$O$_{7-x}$ single layer dc superconducting quantum interference device (SQUID) magnetometer based on bicrystal junctions with 30° misorientation angle, *Appl. Phys. Lett.*, Vol. 72, No. 2, pp. 203-205.

Cantor, R., Lee, L. P., Teepe, M., Vinetskiy, V., & Longo, J. (1995). Low-noise single-layer YBa$_2$Cu$_3$O$_7$ DC-SQUID magnetometers at 77 K, *IEEE Trans. Appl. Supercond.*, Vol.5, No. 2, pp. 2927-2930.

Chen, K.-L., Yang, H.-C., Ko, P. C., & Horng H. E. (2010). Characterization of dual high transition temperature superconducting quantum interference device first-order planar gradiometers on a chip, *J. Appl. Phys.*, Vol.108, pp.064503(4).

Chwala, A., Stolz, R., Ramos, J., Schultze, V., Meyer, H.-G., & Kretzschmar, D. (1999). An HTS dc SQUID system for geomagnetic prospection, *Supercond. Sci. Technol.*, Vol.12, pp.1036–1038.

Clarke, J., & Braginski, A. I., (Editors) (2006). *The SQUID Handbook Vol.2: Applications of SQUIDs and SQUID systems*, (Weinheim: WILEY-VCH Verlag GmbH&Co. KGaA), ISBN 3-52740408-2.

Clem, T. R., Overway, D. J., Purpura. J. W., Bono, J. T., Koch, R. H., Rozen, J. R., Keefe, G. A., Willen, S., & Mohling. R. A. (2001). High-T_c SQUID gradiometer for mobile magnetic anomaly detection, *IEEE Trans. Appl. Supercond.*, Vol.11, pp.871-875.

Daibo, M., Shikoda, A., & Yoshizawa, M. (2002). Non-contact evaluation of semiconductors using a laser SQUID microscope, *Physica C*, Vol.372–376, No.1, pp.263–266.

Daibo, M., & Kamiwano, D. (2005). Examination of relationship between resistivity and photocurrent induced magnetic field in silicon wafers using laser SQUID, *IEEE Trans. Appl. Supercond.*, Vol.15, No. 2, pp. 684-687.

Dam, B., Koeman, N. J., Rector, J. H., Stäuble-Pümpin, B., Poppe, U., & Griessen, R. (1996). Growth and etching phenomena observed by STM/AFM on pulsed-laser deposited $YBa_2Cu_3O_{7-\delta}$ films, *Physica C*, Vol.261, pp.1-11.

Dam, B., Huijbregtse, J. M., & Rector, J. H. (2002). Strong pinning linear defects formed at the coherent growth transition of pulsed-laser-deposited $YBa_2Cu_3O_{7-\delta}$ films, *Phys. Rev. B*, Vol. 65, pp.064528(8).

Dantsker, E., Ludwig, F., Kleiner, R., Clarke, J., Teepe, M., Lee, L. P., Alford, N. McN., & Button, T. (1995). Addendum: ''Low noise $YBa_2Cu_3O_{7-x}$ – $SrTiO_3$ – $YBa_2Cu_3O_{7-x}$ multilayers for improved superconducting magnetometers'', *Appl. Phys. Lett.*, Vol.67, No. 5, pp. 725-726.

David, B. R., Grundler, D., Eckart, R., Fanghänel, K., Krumme, J.P., Doormann, V., & Dössel, O. (1994). A multi-layer process for the fabrication of HTSC flux transformers and SQUIDs, *Supercond. Sci. Technol.*, Vol.7, pp.287–289.

Dogan, O. (2005). The effect of duration of diffusion on Ag diffusion coefficients in $YBa_2Cu_3O_7$, *Journal of Quantitative Spectroscopy & Radiative Transfer*, Vol.95, pp.263-269.

Drung, D., Ludwig, F., Müller, W., Steinhoff, U., Trahms, L., Koch, H., Shen, Y. Q., Jensen, M. B., Vase, P., Holst, T., Freltoft, T., & Curio, G. (1996). Integrated $YBa_2Cu_3O_{7-x}$ magnetometer for biomagnetic measurements, *Appl. Phys. Lett.*, Vol.68, 1421.

Elekta Neuromag® (2006). System description – magnetoencephalographic and electroencephalographic System, NM21761B-A, pp.1-32.

Enpuku, K., Tokita, G., Maruo, T., & Minotani, T. (1995). Parameter dependencies of characteristics of a high-T_c dc superconducting quantum interference device, *J. Appl. Phys.*, Vol.78, pp.3498 – 3503

Enpuku, K., Maruo, T., & Minotani, T. (1996). Effect of large dielectric constant of SrTiO3 substrate on the characteristics of high T_c dc superconducting quantum interference device, *J. Appl. Phys.*, Vol.80, No.2, pp.1207 – 1213.

Enpuku, K., Minotani, T., Shiraishi, F., Kandori, A., & Kawakami, S. (1999). High T_c DC SQUID utilizing bicrystal junctions with 30 degree misorientation angle, *IEEE Trans. Appl. Supercond.*, Vol. 9, No. 2, pp. 3109-3112.

Enpuku, K., Tokimizu, D., Kuroda, D., & Hijiya, S. (2001). A four-junction switch for controlling the opening and closing of a pickup coil in high-T_c superconducting quantum interference device magnetometer, *Jpn. J. Appl. Phys.* Vol. 40 pp.L869–L871.

Enpuku, K., Kuroda, D., Tokimizu, D., & Yang., T. Q. (2002). Suppression of thermally activated flux entry through a flux dam in high-Tc superconducting quantum interference device magnetometer, *J. App. Phys.*, Vol.92, No.8, pp. 4751- 4757.

Espy, M. A., Matlachov, A. N., Volegov, P. L., Mosher, J. C., & Kraus, Jr. R. H. (2005). SQUID-based simultaneous detection of NMR and biomagnetic signals at ultra-low magnetic fields, *IEEE Trans. Appl. Supercond.*, Vol.15, No. 2, pp. 635-639.

Espy, M., Flynn, M., Gomez, J., Hanson, C., Kraus, R., Magnelind, P., Maskaly, K., Matlashov, A., Newman, S., Owens, T., Peters, M., Sandin, H., Savukov, I., Schultz,

L., Urbaitis, A., Volegov P., & Zotev V. (2010). Ultra-low-field MRI for the detection of liquid explosives, *Supercond. Sci. Technol.*, Vol.23, No.3, pp. 034023 (8).

Fagaly, R. L. (2006). Superconducting quantum interference device instruments and applications, *Rev. Sci. Instr.*, Vol.77, pp.101101(45).

Faley, M. I., Gershenson, M.E., Kuchta, N.P. & Salun, V.S. (1991). The "in-situ" preparation and properties of Y-Ba-CuO thin films on the $SrTiO_3$, Al_2O_3 and Si substrates, *IEEE Trans. Mag.* Vol.27, No.2, pp.1475-1478.

Faley, M. I., Poppe, U., Soltner, H., Jia, C.L., Siegel, M., & Urban, K. (1993). Josephson junctions, interconnects and crossovers on chemically etched edges of $YBa_2Cu_3O_7$, *Appl. Phys. Lett.*, Vol.63, pp.2138-2140.

Faley, M. I., Poppe, U., Urban, K., Hilgenkamp, H., Hemmes, H., Aarnink, W., Flokstra, J., & Rogalla, H. (1995). Noise properties of dc-SQUIDs with quasiplanar YBa2Cu3O7 Josephson junctions, *Appl. Phys. Lett.*, Vol.67, No.14, pp.2087-2089.

Faley, M. I., Poppe, U., Jia, C.L., & Urban, K. (1997a). Size, Order and Interface Effects in $YBa_2Cu_3O_7$-$PrBa_2Cu_3O_7$-$YBa_2Cu_3O_7$ Josephson Junctions, *IEEE Trans. Appl. Supercond.*, Vol.7, No.2, pp.2514-2517.

Faley, M. I., Poppe, U., Urban, K., Krause, H.-J., Soltner, H., Hohmann, R., Lomparski, D., Kutzner, R., Wördenweber, R., Bousack, H., Braginski, A. I., Slobodchikov, V. Yu., Gapelyuk, A. V., Khanin, V. V., & Maslennikov, Yu. V. (1997b). DC-SQUID magnetometers and gradiometers on the basis of quasiplanar ramp-type Josephson junctions, *IEEE Trans. Appl. Supercond.*, Vol.7, No.2, pp.3702-3705.

Faley, M. I., Poppe, U., Urban, K., Paulson, D. N., Starr, T., & Fagaly, R. L. (2001). Low noise HTS dc-SQUID flip-chip magnetometers and gradiometers, *IEEE Trans. Appl. Supercond.*, Vol.11, No.1, pp.1383-1386.

Faley, M. I., Poppe, U., Urban, K., Slobodchikov, V. Yu., Maslennikov, Yu. V., Gapelyuk, A., Sawitzki, B., & Schirdewan, A. (2002). Operation of high-temperature superconductor magnetometer with submicrometer bicrystal junctions, *Appl. Phys. Lett.*, Vol.81, No.13, pp.2406-2408.

Faley, M. I., Pratt, K., Reineman, R., Schurig, D., Gott, S., Sarwinski, R. E., Paulson, D. N., Starr, T. N., & Fagaly R. L. (2004). HTS dc-SQUID micro-susceptometer for room temperature objects, *Supercond. Sci. Technol.*, Vol.17, pp.S324-S327.

Faley, M. I., Mi, S. B., Petraru, A., Jia, C. L., Poppe, U. & Urban, K. (2006a). Multilayer buffer for high-temperature superconductor devices on MgO, *Appl. Phys. Lett.*, Vol.89, No.8, pp.082507(3).

Faley, M. I., Jia, C. L., Houben, L., Meertens, D., Poppe, U., & Urban, K. (2006b). Meandering of the grain boundary and d-wave effects in high-T_c bicrystal Josephson junctions, *Supercond. Sci. Technol.*, Vol.19, pp.S195–S199.

Faley, M. I., Mi, S. B., Jia, C. L., Poppe, U., Urban, K., & Fagaly, R. L. (2008). Epitaxial thick film high-T_c SQUIDs, *Journal of Physics: Conf. Ser.*, Vol.97, pp.012164(6).

Faley, M. I., Poppe, U., Urban, K. & Fagaly, R. L. (2010). Noise analysis of dc-SQUIDs with damped superconducting flux transformers, *Journal of Physics: Conf. Ser.*, Vol.234, pp.042009(15).

Faley, M. I., & Poppe, U. (2010a). Sputterquellen für Hochdrucksputtern mit großen Targets und Sputterverfahren, *Patent pending*, DE 102010049329, 22 pages.

Faley, M. I., Poppe, U., Urban, K., & Fagaly, R.L. (2010b). Noise analysis of dc-SQUIDs with damped superconducting flux transformers, *Journal of Physics: Conf. Ser.*, Vol.234, pp.042009(15).

Faley, M. I. (2010c). Cuprate high-T_c superconductors, Chapter in the lecture notes of the 41st IFF Spring School "Electronic Oxides: Correlation Phenomena, Exotic Phases, and Novel Functionalities", 08 - 19 March 2010, Forschungszentrums Jülich, Germany Schriften des Forschungszentrums Jülich, Vol.37, C4 (36 pages) ISSN 1866-1807, ISSN 978-3-89336-609-5.

Fisher, B., Genossar, J., Patlagan, L., Reisner, G. M., Subramaniam, C. K., & Kaiser, A. B. (1994). Hopping conductivity in fully oxygenated $PrBa_2Cu_3O_y$, $YBa_2Cu_2CoO_y$, and $PrBa_2Cu_2CoO_y$, *Phys. Rev. B*, Vol.50, pp.4118–4124.

Hammond, R. H. & Bormann, R. (1989). Correlation between the in situ growth conditions of YBCO thin films and the thermodynamic stability criteria, *Physica C*, Vol.162-164, pp.703-704

Hilbert, C., Clarke, J., Sleator, T., & Hahn, E. L. (1985). Nuclear quadrupole resonance detected at 30 MHz with a DC SQUID, *Appl. Phys. Lett.*, Vol. 47, pp. 637–639.

Hilgenkamp, H., & Mannhart, J. (2002). Grain boundaries in high-T_c superconductors, *Rev. Mod. Phys.*, Vol.74, pp.485-549.

Gross, R., Alff, L., Heck, A., Froehlich, O. M., Koelle, D., & Marx, A. (1997). Physics and technology of high temperature superconducting Josephson junctions, *IEEE Trans. Appl. Supercond.*, Vol.7, No.2, pp.2929-2935.

Grüneklee, M., Krause, H.-J., Hohmann, R., Maus, M., Lomparski, D., Banzet, M., Schubert, J., Zander, W., Zhang, Y., Wolf, W., Bousack, H., Braginski, A. I., & Faley, M. I. (1997). HTS SQUID system for eddy current testing of airplane wheels and rivets, *Review of Progress in Quantitative NDE*, Plenum, N.Y., Vol.17.

Jia, C. L., Faley, M. I., Poppe, U., & Urban, K. (1995). Effect of chemical and ion-beam etching on the atomic structure of interfaces in $YBa_2Cu_3O_7$/$PrBa_2Cu_3O_7$ Josephson junctions, *Appl. Phys. Lett.*, Vol.67, No.24, pp.3635-3637.

Jia C. L., Mi, S.B., Faley, M. I., Poppe, U., Schubert, J., & Urban, K. (2009). Oxygen octahedron reconstruction in the $SrTiO_3$/$LaAlO_3$ heterointerfaces investigated using aberration-corrected ultrahigh-resolution transmission electron microscopy, *Phys. Rev. B*, Vol.79, pp.081405(R)

Khapaev, M. M., Kupriyanov, M. Yu., Goldobin E., & and Siegel M., (2003). Current distribution simulation for superconducting multi-layered structures, *Supercond. Sci. Technol.*, Vol.16, pp.24.

Kim, S. I., Kametani, F., Chen, Z., Gurevich, A., Larbalestier, D. C., Haugan, T., & Barnes, P. (2007). On the through-thickness critical current density of an $YBa_2Cu_3O_{7-x}$ film containing a high density of insulating, vortex-pinning nanoprecipitates, *Appl. Phys. Lett.* Vol.90, pp.252502(3)

Kleiner, R., Koelle, D., Ludwig, F., & Clarke, J. (2004). Superconducting quantum interference devices: state of the art and applications, *Proc. IEEE*, Vol.92, No.10, pp.1534-1548.

Krause, H.-J., Wolf, W., Glaas, W., Zimmermann, E., Faley, M. I., Sawade, G., Mattheus, R., Neudert, G., Gampe, U., & Krieger, J. (2002). SQUID array for magnetic inspection of prestressed concrete bridges, *Physica C*, Vol. 368, Issues 1-4, pp.91-95.

Liao, S.-H., Huang, K.-W., Yang, H.-C., Yen, C.-T., Chen, M. J., Chen, H.-H., Horng, H.-E., & Yang, S. Y. (2010). Characterization of tumors using high-T_c superconducting quantum interference device-detected nuclear magnetic resonance and imaging, *Appl. Phys. Lett.*, Vol. 97, pp.263701(3).

Ludwig, C., Kessler, C., Steinfort, A.J., & Ludwig W. (2001). Versatile High Performance Digital SQUID Electronics, *IEEE Trans. Appl. Supercond.*, Vol.11, No.1, pp.1122-1125.

Matias, V., Rowley, E. J., Coulter, Y., Maiorov, B., Holesinger, T., Yung, C., Glyantsev, V. & Moeckly, B. (2010). YBCO films grown by reactive co-evaporation on simplified IBAD-MgO coated conductor templates, *Supercond. Sci. Technol.*, Vol.23, pp.014018(5).

Mi, S. B., Jia, C. L., Faley, M. I., Poppe, U., & Urban K. (2007). High resolution electron microscopy of microstructure of $SrTiO_3$/$BaZrO_3$ bilayer thin films on MgO substrates, *J. Crystal Growth*, Vol.300, pp.478-482.

Minotani, T., Kawakami, S., Kuroki, Y., & Enpuku, K. (1998). Properties of Josephson junction fabricated on bicrystal substrate with different misorientation angles, *Jpn. J. Appl. Phys.*, Vol.37, pp.L718-L721.

Navacerrada, M. A., Lucía, M. L., Sánchez-Quesada, F., & Sarnelli, E. (2008). Fiske steps and hysteresis in $YBa_2Cu_3O_7$ grain boundary Josephson junctions: Structural information of the barrier by means of a non-destructive approach, *J. Appl. Phys.*, Vol.104, pp.113915(6).

Ohtomo, A., & Hwang, H. Y. (2004). A high-mobility electron gas at the $LaAlO_3$/$SrTiO_3$ heterointerface, *Nature*, Vol.427, pp.423-426.

Paladino, A. E. (1965). Oxidation kinetics of single-crystal $SrTiO_3$, *Journal of American Ceramic Society*, Vol.48, No.9, pp.476-478.

Polonsky, S., Semenov, V., & Shevchenko, P., (1991). PSCAN: personal superconductor circuit analyser, *Supercond. Sci. Technol.*, Vol.4, pp.667.

Poppe, U., Schubert, J., & Evers, W. (1990). Method of fabricating thin layers from high temperature oxide superconductors, Patent US4965248.

Poppe, U., Klein, N., Dähne, U., Soltner, H., Jia, C. L., Kabius, B., Urban. K., Lubig, A., Schmidt, K., Hensen, S., Orbach, S., Müller, G., & Piel, H. (1992). Low resistivity epitaxial $YBa_2Cu_3O_7$ thin films with improved microstructure and reduced microwave losses, *J. Appl. Phys.*, Vol.71, pp.5572-5578.

Poppe, U., Faley, M. I., Breunig, I., Speen, R., Urban, K., Zimmermann, E., Glaas, W., & Halling, H. (2004). HTS dc-SQUID microscope with soft-magnetic flux guide, *Supercond. Sci. Technol.*, Vol.17, pp.S191-S195.

Prusseit, W., Furtner, S. & Nemetschek, R. (2000). Series production of large area $YBa_2Cu_3O_7$ films for microwave and electrical power applications, *Supercond. Sci. Technol.*, Vol.13, pp.519-521.

Ryhänen, T., Seppä, H., Ilmoniemi, R., & Knuutila, J. (1989). SQUID magnetometers for low-frequency applications, *J. Low Temp. Phys.*, Vol.76, Nos.5/6, pp.287-386.

Sobol, E. (1995). *Phase transformations and ablation in laser-treated solids*, Wiley, New York.

Song, F., He, M., Faley, M. I., Fang, L., & Klushin, A. M. (2010). Improved coupling of Josephson junction arrays to the open space, *J. Appl. Phys.*, Vol.108, 063903(5).

Tarasov, M., Gudoshnikov, S., Kalabukhov, A., Seppa, H., Kiviranta, M., & Kuzmin, L., (2002). Towards a dc SQUID read-out for the normal metal hot-electron microbolometer, *Physica C*, Vol.368, Issues 1-4, pp.161-165.

Tinkham, M. (1996). *Introduction to Superconductivity*, 2nd edition, McGraw-Hill Inc., New York, ISBN 0-07-064878-6, p.225.

Valentino, M., Ruosi, A., Peluso, G., & Pepe, G. P. (2002). Structural health monitoring of materials by high critical temperature SQUID, *Physica C*, Vol.372-376, No.1, pp.201-208.

Voss, R.F. (1981). Noise characteristics of an ideal shunted Josephson junction, *J. Low Temp. Phys.*, Vol.42, Nos.1/2, pp.151-163.

Watanabe, T., Watanabe, S., Ikeda, T., Kase, M., Sasaki, Y., Kawaguchi, T., & Katayama, T. (2004). A prototype of a highly sensitive cryogenic current comparator with a HTS SQUID and HTS magnetic shield, *Supercond. Sci. Technol.*, Vol.17, pp.S450–S455.

Watanabe, T., Fukunishi, N., Sasaki, Y., Kase, M., Goto, A., & Kamigaito, O. (2010). Development of beam current monitor with high-T_c SQUID at RIBF, *Proceedings of Beam Instrumentation Workshop (BIW10), La Fonda on the Plaza Santa Fe, New Mexico, USA, May 2-6, 2010*, Invited talk, 10 pages.

Winkler, D., Zhang, Y. M., Nilsson, P. A., Stepantsov, E. A., & Claeson, T. (1994). Electromagnetic properties at the grain boundary interface of $YBa_2Cu_3O_{7-\delta}$ bicrystal Josephson junctions, *Phys. Rev. Lett.*, Vol.72, No.8, pp.1260-1263.

Witchalls C. (2010). Nobel prizewinner: We are running out of helium. *New Scientist*. 18 August 2010, Witchalls C. (2010). One minute with... Robert Richardson, *The New Scientist*, Vol.207, Issue 2773, 14 August 2010, p.29.
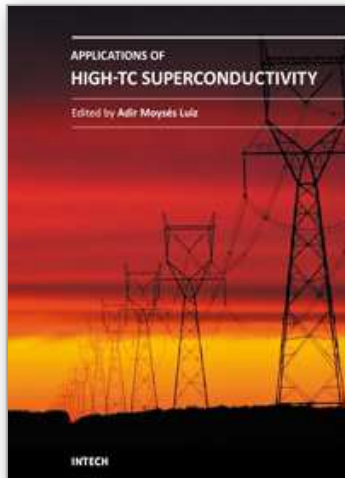
Applications of High-Tc Superconductivity

Edited by Dr. Adir Luiz

This book is a collection of the chapters intended to study only practical applications of HTS materials. You will find here a great number of research on actual applications of HTS as well as possible future applications of HTS. Depending on the strength of the applied magnetic field, applications of HTS may be divided in two groups: large scale applications (large magnetic fields) and small scale applications (small magnetic fields). 12 chapters in the book are fascinating studies about large scale applications as well as small scale applications of HTS. Some chapters are presenting interesting research on the synthesis of special materials that may be useful in practical applications of HTS. There are also research about properties of high-Tc superconductors and experimental research about HTS materials with potential applications. The future of practical applications of HTS materials is very exciting. I hope that this book will be useful in the research of new radical solutions for practical applications of HTS materials and that it will encourage further experimental research of HTS materials with potential technological applications.

How to reference

In order to correctly reference this scholarly work, feel free to copy and paste the following:

Michael Faley (2011). Epitaxial Oxide Heterostructures for Ultimate High-Tc Quantum Interferometers, Applications of High-Tc Superconductivity, Dr. Adir Luiz (Ed.), ISBN: 978-953-307-308-8, InTech, Available from: http://www.intechopen.com/books/applications-of-high-tc-superconductivity/epitaxial-oxide-heterostructures-for-ultimate-high-tc-quantum-interferometers

INTECH

open science | open minds